INFLATABLE WING UAV EXPERIMENTAL AND ANALYTICAL FLIGHT MECHANICS

A Thesis
Presented to
The Academic Faculty

by

Ainsmar Brown

In Partial Fulfillment
of the Requirements for the Degree
M.S. Aerospace Engineering in the
School of Aerospace Engineering

Georgia Institute of Technology
May 2011

INFLATABLE WING UAV EXPERIMENTAL AND ANALYTICAL FLIGHT MECHANICS

Approved by:

Dr. Eric Johnson, Advisor
School of Aerospace Engineering
Georgia Institute of Technology

Dr. Dewey Hodges, Co-Advisor
School of Aerospace Engineering
Georgia Institute of Technology

Dr. John-Paul Clarke
School of Aerospace Engineering
Georgia Institute of Technology

Date Approved: January 14, 2011

To my mother and Brooklyn, NY.

ACKNOWLEDGEMENTS

I wish to thank The Army Research Lab and Harris Edge for the continued support on a multitude of levels. I would also like to thank Howard Carpenter for the technical advise and assistance on the design and build of the experimental platform. Thank you as well, Howard, for being a great pilot. In addition, I extend thanks to Allistair Moses and Zahra Sotoudeh for their shared expertise in embedded programming and the NATASHA code, respectively. Thank you kindly, Arizona Balloon Company for the fabrication of the polyurethane wings. I would also like to thank Georgia Tech for providing the Center for Distance Learning, and running it as professionally as they have. The continuity it has allowed me to have between my undergraduate and Master's studies was to my benefit without question.

TABLE OF CONTENTS

	Page
ACKNOWLEDGEMENTS	iv
LIST OF TABLES	vii
LIST OF FIGURES	viii
NOMENCLATRURE	xi
SUMMARY	xiv
CHAPTER	
1 INTRODUCTION	1
1.1 Motivation	1
1.2 Goals	3
1.3 Thesis Outline	4
2 LITERATURE REVIEW	6
2.1 Airships and Balloons	6
2.2 Low Mass Modeling	8
2.3 Nonlinear Effects	9
2.4 Previous Designs	10
2.5 Structural Dynamics	12
2.6 Use of Feedback Control	13
3 THEORETICAL BACKGROUND	15
3.1 Baseline Model	15
3.2 Flight Dynamics	22
3.3 NATASHA Model	27

4 EXPERIMENTAL SETUP 32

4.1 Modifying an existing platform 32

4.2 Foam electric plane 37

4.3 Autopilot 42

5 RESULTS 44

5.1 Longitudinal Dynamics Model 44

5.2 NATASHA 58

6 CONCLUSIONS 63

6.1 Summary 63

6.2 Recommended Future Work 64

APPENDIX A: MATLAB CODE AND PSEUDO-CODE 65

APPENDIX B: PLATFORM DATA AND DIAGRAMS 80

APPENDIX C: ADDITIONAL RESULTS FROM ANALYSIS 82

REFERENCES 86

LIST OF TABLES

Table 4.1: Wing tip deflections 34

Table 5.1: Z coefficients 45

Table 5.2: X coefficients 45

Table 5.3: Moment coefficients 45

Table 5.4: Experimental data on cantilevered wing without supporting structures 62

Table B.1: Additional platform description 80

Table B.2: Vehicle approximated inertia tensor with rigid wing in lbs-ft 80

Table C.1: First 10 bending modes in NATASHA for cantilevered wing in vacuum 82

Table C.2: First 10 bending modes in NATASHA for cantilevered wing in vacuum 82

Table C.3: Example results from coefficient tuning 84

Table C.4: Error propagation sources 85

LIST OF FIGURES

Page

Figure 1: ILC Dover Aperton flying wing UAV 2

Figure 2: Goodyear Inflatoplane 3

Figure 3: Step response for rigid B-1 model 17

Figure 4: Step response for flexible B-1 model 17

Figure 5: Magnitude and phase plot for rigid B-1 model 18

Figure 6: Magnitude and phase plot for flexible B-1 model 18

Figure 7: Variation of inflow state 1 with increased number of inflow states 21

Figure 8: Wing cross-section 28

Figure 9: Elliptic lift distribution 28

Figure 10: Loads idealization 29

Figure 11: Cantilevered beam simplification 29

Figure 12: Torsional load idealization 30

Figure 13: Wing supports 33

Figure 14: Pull test setup 33

Figure 15: Frequency response of the elevator to pitch angle bare airframe dynamics 35

Figure 16: Frequency response of the elevator to pitch rate bare airframe dynamics 35

Figure 17: Data-logging diagram 36

Figure 18: Experimental platform 37

Figure 19: Experimental platform propeller and wing mounting detail 38

Figure 20: Rendering of CAD model used for approximating the mass model 39

Figure 21: Lift coefficient plot for Polyurethane wing 40

Figure 22: Example GPS plot of the glider's cross-range flight path 40

Figure 23: Example GPS total velocity plot for a given flight 41

Figure 24: Dorsal fin for roll stability 42

Figure 25: ARL/UAH Open Autopilot used to obtain results 43

Figure 26: Control input to elevator 46

Figure 27: Theta for wing with supports 46

Figure 28: Error plot for wing with supports 47

Figure 29: Simulation cross-range 47

Figure 30: Euler angles for no supports 48

Figure 31: PWM for flight with no supports 48

Figure 32: Accelerations for wing with no supports 49

Figure 33: Control input for second case at 4 Hz 50

Figure 34: Theta for wing without supports 50

Figure 35: Error for theta for wing without supports 51

Figure 36: Rigid wing flight test elevator input 51

Figure 37: Rigid wing theta Euler angle response for flight test and simulation model 52

Figure 38: Flat wing elevator input with a single support inflated with helium and augmented with vertical fin before turn 52

Figure 39: Flat wing theta angle response with a single support inflated with helium and augmented with vertical fin before turn 53

Figure 40: Error plot for flat wing theta angle response with a single support inflated with helium and augmented with vertical fin before turn 53

Figure 41: Bending mode dampens pitching motion 54

Figure 42: Comparison of model error when doubling the value of $C_{M\eta}$ 54

Figure 43: Finned straight wing performing a turning maneuver 55

Figure 44: Magnitude and phase plot for simulation matching wing with a single support 56

Figure 45: Magnitude and phase plot for simulation matching flat wing without supports 57

Figure 46: System ID of flight test data for single spar 58

Figure 47: Forces from first bending model in NATASHA 60

Figure 48: Phasing from forces of the first bending mode in NATASHA 60

Figure 49: Moments from first bending mode in NATASAHA 60

Figure 50: Phasing from moments of the first bending mode in NATASHA 61

Figure B.1: Glider drawing with dimensions 81

Figure C.1: 2nd bending mode of cantilevered wing 83

Figure C.2: 3rd bending mode of cantilevered wing 83

Figure C.3: 4th bending mode of cantilevered wing 83

Figure C.4: 5th bending mode of cantilevered wing 83

Figure C.5: 6th bending mode of cantilevered wing 83

Figure C.6: 7th bending mode of cantilevered wing 83

Figure C.7: 8th bending mode of cantilevered wing 84

Figure C.8: 9th bending mode of cantilevered wing 84

Figure C.9: 10th bending mode of cantilevered wing 84

Figure C.10: Example plots from the coefficient tuning process 85

NOMENCLATRURE

α	Angle of attack
Δ	Perturbation
δ	Control input
ϵ	Strain
κ	Twist
η	Wing bending mode
ϕ	Euler roll angle
θ	Euler pitch angle
ψ	Euler yaw angle
ρ	Density (Air)
ν	Linear velocity
ω	Natural frequency/Angular velocity
AR	Aspect ratio
C	Aerodynamic coefficient
E	Elastic Modulus
F	Force
G	Shear Modulus
I	Moment of Inertia
L	Length
M	Moment
Q	Generalized force

S	Wing area
T	Kinetic Energy
U	body x velocity component
V	body y velocity component
W	body z velocity component / weight
b	Wing span
c	Chord
g	Local gravitational acceleration
i	Angle of incidence
m	Mass / pitching moment
p	roll rate
q	pitch rate/ Motion variable
r	yaw rate
s	Laplace domain variable
t	Wing thickness
ADC	Analog to digital converter
AIAA	American Institute of Aeronautics and Astronautics
CAD	Computer Aided Design
HALE	High Altitude, Long Endurance
PWM	Pulse width modulation
the	“Theta”, or body pitching component
UAS	Unmanned Air System

Subscripts/ Superscripts

1	first mode/ misc.
e	elevator
o	initial condition/ steady-state
x	x-direction component, skew symmetric matrix
y	y-direction component
z	z-direction component

SUMMARY

The field of man portable UASs (Unmanned Aerial Systems) is currently a key area in improving the fielded warrior's capabilities. Pressurized aerostructures that can perform with similar results of solid structures can potentially change how this objective may be accomplished now and in the future. Construction with high density polymers and other composites is currently part of active inflatable vehicle research. Many shape forming techniques have also been adapted from the airship and balloon manufacturing industry. Additional research includes modeling techniques so that these vehicles may be included in simulation packages.

A flight dynamics simulation with reduced-order aeroelastic effects derived with Lagrangian and Eulerian dynamics approaches were developed and optimized to predict the behavior of inflatable flexible structures in small UASs. The models are used to investigate the effects of significant structural deflections (warping) on aerodynamic surfaces. The model also includes compensation for large buoyancy ratios. Existing literature documents the similarity in structural dynamics of rigid beams and inflatable beams before wrinkling. Therefore, wing bending and torsional modes are approximated with the geometrically exact intrinsic beam equations using NATASHA (Nonlinear Aeroelastic Trim And Stability for HALE Aircraft) code. An approach was also suggested for inclusion of unique phenomena such as wrinkling during flight. A simplified experimental setup will be designed to examine the most significant results observed from the simulation model. These methods may be suitable for specifying limits on flight maneuvers for inflatable UASs.

This page is intentionally left blank.

CHAPTER 1

INTRODUCTION

1.1 Motivation

UAVs have become an undeniable factor in modern technology in both commercial and military arenas. All branches of the department of defense maintain a rigorous unmanned vehicles program. Within the United States Army, unmanned air and ground vehicles have been integrated into everything from explosive ordinance disposal, to search and rescue. In order to expand the usability of these platforms, basic and applied research into the expanded capabilities of these technologies has become front and center.

Unmanned technologies has proven to be an effective way of expanding the capabilities of the dismounted soldier. Currently, a solider may expect to carry up to 70 pounds of additional equipment as part of his outfitting. At the same time, today's solider has few options for an eye in the sky in spite of all of that payload. One way to fill in the gap in this capability is to provide the soldier with a down-link from a air reconnaissance platform. However, these resources are limited. Therefore, the concept of a personal air vehicle has become attractive in recent years. In order to mitigate the obvious payload penalty on the individual in the field, reduced mass and light-than-air vehicles have been proposed [1]. These platforms would be able to take up less volume by rolling up tightly for storage, and they would also weight less under most circumstances. A variety of platforms would potentially fit in this category, but then there is the trade-off with how much additional resources would be necessary to make these newer systems comparable to the rugidized hardware and software that exists in the field today.

Lighter than air vehicles such as balloons and blimps are mature technologies, but require a source to fill a large volume with air or helium. Therefore, the inflatable wing platform is proposed as an option that would make a compromise between all of these factors mentioned. The smaller volume of the inflatable wing would require much less air or helium and could potentially just be blown up my mouth in the field within 2-3 minutes.

Depending on the desired level of reinforcement and cost of materials to fabricate the wings, the structural qualities of the aircraft will vary and the flight dynamics associated with them would follow. One example of such an aircraft is given in figure 1, discussed later in the literature review, chaper 2. This manuscript provides the concept of a notional platform and discusses the effect that such design variability might bring.

The inflatable vehicle is not new to the United States Army as is evidenced by figure 2 below showing the Goodyear Inflatoplane [2] which was designed to be used after World War II. It was the hope of the designers that the vehicle could be used to provide short range search and rescue platforms of pilots who had been shot down by enemy fire. Eventually the project was canceled as the Army later determined that the inflatable nature of the vehicle was too susceptible to an easy take down by this same enemy fire.

Figure 1: ILC Dover's Aperton UAV

Figure 2: Goodyear Inflatoplane

1.2 Goals

In this thesis, the major objectives are as follows:

- Describe the relevant phenomena that would make the notional inflatable wing aircraft designed for the dismounted soldier different from the standard platform.
- Develop a simulation model that contains the essential elements for longitudinal flight data matching. Discuss pertinent issues related to the lateral dynamics as well.
- Design and build a platform suitable for capturing flight test data which is capable of showing the difference between a more conventional fixed wing design and the notional inflatable wing design that would exhibit more flexibility in a non-trivial fashion.
- Perform the frequency decomposition of flight data to provide comparative information on the modes, vehicle control bandwidth and the any resonant frequencies that change based on the flexibility of the wing.

- Provide enough information on each wing configuration as far as design and structural properties so that the data in this thesis may be extrapolated to other cases in the future.
- Match simulation data to the flight test data for a selection of design points.
- Determine from model matching the most critical model parameters in making the model match the flight test data as closely as possible.

1.3 Thesis Outline

The organization of the remainder of this thesis is as follows:

- The literature review in chapter 2 presents a broad discussion on all relevant material to the concept of an inflatable UAV. References are made to documents discussing the relevant analytical content that is deemed useful. Reference is also made to examples of real aircraft described in the literature to explain where the technology currently sits and show where the gaps exists in current literature.
- The theoretical background in chapter 3 is designed to provide detail explanations on the basic principals used to describe the notional inflatable wing aircraft. In addition to this, any unique formulations relevant to the models and experimental platforms in this thesis are presented.
- Chapter 4 presents the experimental setup section. Here, the purpose of the physical glider test is explained. All of the equipment used as well as the methods used to capture the test data is presented.
- Following the discussion on the foundational work, chapter 5 presents the results from both the experimental and the analytical studies are presented and explained. As a whole, they provide the complete view of the most important gains made from the research contained in this work.

- The thesis ends in chapter 6 with a conclusion to summarize the results of the thesis and suggestions are made on what future work would be most useful. Work that will likely grow out from the results is also presented. The appendices follow which include excerpts of the most important code written specifically for this research.

CHAPTER 2

LITERATURE REVIEW

The following presents major research related to the topics covered in inflatable winged UAVs. Background information includes research related to theoretical vehicle flight mechanics as well as wing and vehicle design.

2.1 Airships and Balloons

The subject of inflatable aircraft crosses several basic disciplines of engineering mechanics. For instance, some of the aerodynamic interactions are discussed in the growing work of manned and unmanned airships and aerostats. The sizes of these unmanned vehicles generally range from 5 to 15 feet in length and have found great utility in many university research programs [3]. Others have been designed on a scale exceeding 100 ft in length, where the designs are essentially the same as full scale manned airships. However, as is the case in [3, 4], these research topics tend to exploit the relatively slow nominal dynamics of these vehicles and focus on the lighter-than-air platforms as vessels for research in sensing or autonomy.

In some of the more recent research, some of these neglected areas have seen more attention. In [5], Kornienko, devised a detailed process for using system identification to model airship dynamics. His approach was mutli-tiered starting from complex analytical models, simplifying these models to aid in parameter identification, and devising proper flight test maneuvers so that the information of interest would show up in the test data. Linear models were eventually used to make the physical information more tractable to system identification. A combination of the Filter Error method and the Output Error method was used to come up with the optimal interpretation of the experimental data. The finals results were synthesized into the vehicle linear models. Additionally, the airship modeling was based on a non-standard model where the

influence of wind was modeled in a unified approach, acting as another subsystem of the overall modeling environment. Lagrangian dynamics were used to model the airship mechanics, the air control volume mechanics surrounding the airship and the energy transfer between the airship and surrounding control volume. The equations of motion were then transformed to the traditional Newton-Euler equations of motion. Root-locus analysis showed that the pole movement remained minimal in the given range of gust responses.

Later, Li [6] demonstrated perhaps the most elaborate flight dynamics model and validated the information with existing test data for the subject platform. This was an approach to incorporate aerostatics, aerodynamics, structural dynamics, and flight dynamics into a single modeling scheme. Li used the Free-Free Euler-Bernoulli beam model to represent the structural dynamics of the airship hull. The ellipsoidal shape of the hull easily lent itself to the potential flow models often used in airship dynamics. These potential flow equations had originally been derived in the canonical text by Lamb [7] and later applied to airships [8] and underwater vehicles [9]. Even with the nearly ideal ellipsoidal shape of an airship, these analytical formulations still proved to be incomplete, as also noted by Li, thus furthering the imperative for experimental data.

Winged inflatable aircraft will deviate from many of the principals of standard airship design. As explained in Khory and Gillett [10], even hybrid versions of these platforms, such as the NASA Ames Megalifter, will endure larger aerodynamic loads at higher speeds than similarly sized airships. Additional structure must therefore be added to make the frame structurally sound. This may be done through the use of thicker fabrics or through the use of optimized geometry such as is the case with the cellular wing design concept. The shape of these aircraft are less volumetrically efficient, usually to allow the frame to experience lower drag loads at higher speeds. These two characteristics imply that inflatable winged aircraft will almost always fall well short of neutral buoyancy.

In the aerospace industry, much work has been done on space structural dynamics that are inflatable and tend to be highly flexible [11]. Much of the readily available information on flight control of flexible structures is directly related to space structures due to the relaxed non-atmospheric conditions [12]. The introduction of atmospheric interactions present a completely new set of problems.

2.2 Low Mass Modeling

Additional factors make modeling an inflatable winged aircraft difficult. Research that discusses the behavior of a low mass, high volume wing may be found in the modeling of parafoil dynamics and aerodynamics. The area of unmanned parafoils has received significant attention from the academic, commercial and military sectors [13, 14]. Parafoils are considered inexpensive platforms that are efficient in delivering payloads of various sizes from air to ground. Inflatable winged aircraft, may be considered an extension on the current capabilities of unmanned parafoils which are designed for gliding flight. Several authors have investigated various aspects of parafoil flight dynamics for unmanned use, including Slegers and Costello [15, 16]. In their paper, the issue of limited control and the onset of instability from warping the profile of the parafoil was addressed. Slegers and Costello also included compensation for variable geometry in modeling parafoil trajectories. Parafoils are not generally pre-inflated with air or any lighter than air gas; however, in order for their descent to be controlled, large semi-static deflections must be induced to change the aerodynamics properties and provide the control desired by the pilot or autopilot. In addition, parafoils share the same property of having low mass-to-volume ratios, which makes the principals of added mass and inertia non-negligible.

Inflatable winged UAVs made of some of the more flexible materials present nontrivial problems in aeroelasticity. It has been documented that flexible inflated structures will behave much like solid flexible structures prior to the onset of surface

wrinkling [17]. Some of the analytical results; however, broke down for beams of insufficient length to diameter ratios (L/D < 6), emphasizing the importance of the appropriate assumptions in the modeling process. Various topics from time varying linear modeling, 2-D strip theory, to stability and control of unstable aeroelastic models, have seen years of research for traditional fixed-winged aircraft. Much of this background was documented in the dissertation by Raghavan [18]. Like others before, the results from the dissertation by Ragahavan was not tested on a physical platform, but instead were validated with high fidelity simulations that have previously undergone some level of validation of their own.

Another paper discusses the combination of beam mechanics and yarn (plate) mechanics [19]. In the paper by Su and Cesnik [20], the reduction in torsional stiffness due to wing bending was identified as a biliniar effect. A switching setup was implemented to include this change in the strength properties of the aircraft's wing. Patil and Hodges [21] predicted the disappearance of the short period mode of a trimmed HALE aircraft. They also showed the increased instability of the phugoid mode when the payload was increased for this vehicle. It is reasonable to expect that designs of an inflatable winged aircraft would include wingspans long enough to be susceptible to similar effects if they are to have the endurance similar to modern fielded aircraft such as the Aerovironment Raven and Puma AE which is designed for a 2 hour endurance [22].

2.3 Nonlinear Effects

Some of the earliest work to attempt unified flight dynamics models that provided information on vehicle stability include works by Meirovich and Tuzcu [23]. This works compared several approaches that placed different weights of importance on the rigid body modes and on the flexible aeroelastic modes. After carrying out the modal analysis it became clear that the unified approach was the most appropriate when considering the information that was lost using simpler formulations. Meirovich and Tuzcu also proposed

methods for reducing the computational time of these models. Coefficient estimation works well around the nominal trim condition, as is outlined in textbooks such as Etkin [24]. Others have treated aeroleastic effects like perturbations near the nominal condition such as Bennachur, et al. [25]. This approach may be successful if the aeroelastic effects remain minimal as they often do on highly pressurizes airships.

2.4 Previous Designs

Pressurized wing aircraft have seen various designs over the years with different fabrics and composites. One of the earliest designs of note included the Goodyear manned aircraft used as a field assembled pilot rescue platform [2]. The ILC Dover company has researched this area for the last 40 years and has numerous publications about construction techniques and vehicle design around pressurized wings [26]. The Apteron design from the 1970s used a tailless design with hard control surfaces attached to the wing. Modern designs have adopted similar design principals. This approach includes cells, or baffles, which section off individual units within the wing and retain their pressure with simplified shapes such as cylinders. A combination of these cylinders with the proper sizing and intervals allow for an overall structure that behaves, for the most part, like a wing designed from an airfoil with continuous curves. Differences that have been noted include less flow separation at lower flight speeds for the cellular wing, with the trade-off of a more unsteady flow field [27]. Additional analytical work from ILC Dover, supported by the University of Kentucky, has shown Finite Element Analysis (FEM) results for the purpose of functional wing warping [28]. This warping mechanism was intended integrate control surfaces that would serve the purpose of ailerons on the main wing. Additional work on flight testing inflatable wings was done by the University of Kentucky [29, 30]. The approach in this research determined, parametrically, the deflection characteristics of inflatable wings they designed with materials such as Kevlar and Vectran. Some instances of their design mitigated the issue of pressure retention by

designing a material that would cure in sunlight by means of natural UV exposure. With a fairly large design range (10-25 psi, 10-50 Newtons), it was shown that static tip deflections from point loads remained fairly small (less that 3 % span). Their unmanned vehicle was also designed with a camera system built into the vehicle's tail section to capture deflection data of the pressurized main wing during flight. Furthermore, roll stability was affected on these vehicles due to the added dihedral that came from the independent bending of the left and right wing about the mid-span.

More recently, a group of researchers have investigated the passive flight dynamics of tumbling wings [31]. The objective was to obtain more comprehensive information on the mechanics of falling seed pods. Just from the analysis of the passive dynamics, information was gained on the stability of a flat paper wing at different surface densities. The onset of instability of the flat wing configuration was followed by transition to a stable curved configuration; for which, the degree of curvature varied at different decent rates. However, prior to buckling of the wing in tumbling flight, the trajectory of the wing was related to a limited number of parameters. The correlation of geometry to tumble rate lead to the belief that changes in inertia may not have quite as direct an effect on the modes that appear or disappear in a highly flexible wing. As expected, for a given wing cross-section there was a designed critical wingspan; below which, the wing would stay flat, even in the complex nature of tumbling flight, and above which, the wing would experience instability in its configuration and buckle to a new equilibrium curvature.

As was the case with the work by Tuzcu and Meirovitch, it was determined that the aeroelastic effects were nontrivial. The recommendation was that the coupled modeling of the rigid flight mechanics and the aeroelasticity was mandatory to obtain results of any true experimental value.

Clarkson University in New York collaborated with researchers at the Imperial College of London to investigate materials and aerodynamic properties of several

inflatable wings. Chang completed a thesis outlining a complete design and analysis process of inexpensive inflatable wing vehicles [32]. His analysis paid particular attention to all the subsystems and what modifications might be beneficial in consideration of the type of platform being deployed. No flyable test vehicle was ever designed, however different wings were fabricated for a series of wind tunnel tests.

2.5 Structural Dynamics

The dissertation by Reshke in 2006 [33] focused on the dynamics for structural loads. As a result, emphasis was placed on turbulence models. The code structure was tailored towards the integration of Finite Element models. As was eventually seen in several other models, a mean axis formulation was used for the load reference point of the vehicle dynamic model. The work by Patil [34] focused more on beam mechanics. It took into account beam anisotropy and geometric nonlinearities. Dynamic stall was looked at under unsteady flow conditions. Shearer [35] used a virtual work model for the rigid body loads as well as the flexible modes. The new models were computed under different numerical integration methods including a modified Newmark method for 1st order and 2nd order ODE solutions. In 2007, a dissertation by Looye [36] at TU Delft took many of the modern results for aeroelastic models and implemented them in a flight simulator environment to evaluate pilot handling qualities. A similar model was used in work published a year later by Reijerkerk [37]. This model was tailored for static aerelasticity for the purpose of modeling the in-flight behavior of various winglet designs. This model used the method published in Waszak and and Schmidt [38] as the starting point but also implemented a variety of alternative aerodynamics models including vortex-lattice method. The same year, Su [39] from the University of Michigan published a dissertation for reduced order, nonlinear strain-based FE models that made use of the Peter's inflow model. Models derived with similar levels of rigor were published by Chang in 2006 [40] for total vehicle vibration modes.

2.6 Use of Feedback Control

Lastly, though detailed work on feedback control is not included here, significant research has been done on the control aspects of inflatable aircraft, and even more so, on highly flexible aircraft. The field can be split into the subjects of control surface actuator design and propulsion design. ILC Dover and the University of Kentucky have documented implementation of servomotor devices on the surface of their inflatable wings. These devices were used to investigate the roll control mechanism that was previously mentioned. These actuators were also integrated to test airfoil reconfiguration to see if the use of different 2-D profiles could be switched dynamically and make the surface more efficient in different regimes of flight [41, 42]. Dozens of flight test where conducted to find gains acceptable for a standard PID based autopilot integrated into the test vehicle. During the take-off phase, it was also noted that the induced added dihedral of the inflatable wings contributed to an undesirable dutch-roll mode. Nothing has yet been documented that addresses this problem. Research has since continued with the inclusion Piezoelectric actuators in place of the servo motor actuators.

A paper in 2008 by Shearer and Cesnik [43], proposing a method for trajectory control of flexible wing aircraft, a common approach, where a fast inner-loop controller is used to maintain stability of the aeroelastic modes, while a slower outer-loop controller incorporating feedback linearization controlled the rigid body modes of the vehicle.

Within the analysis, it was noted that time delays between the control input and the actual vehicle state response created a nonminimum phase system, thus increasing the difficulty outer-loop control. Feedback was shifted from altitude control to desired trajectory to preserve the usability of the control architecture. Several authors have looked into robust control applications to account for model order truncation, which aides in simplifying designs of model following feedback controllers. In these instances, the

number of states can grow considerably when the aeroelastic states are taken into consideration of a flight dynamics model. In [44] a μ - synthesis controller was used to take into account the general uncertainty of the model as well as the residuals that arise from model-order and control-order reduction. The results were satisfactory for a B-52 flight dynamics model.

Lastly, Palacios and Cesnik [45], aware of the growing number of approaches available for modeling mechanics of highly flexible aircraft, did a comparative analysis of different beam modeling techniques for both wing and fuselage aeroelasticity. The comparison was made between strain-based beams, intrinsic beams, and displacement beams. The model also used substructuring, favoring the intrinsic beam model for the wings. Lastly, model order reduction was implemented. This paper thus far has been the best comparative study on some of the most popular beam modeling approaches.

CHAPTER 3

THEORETICAL BACKGROUND

3.1 Baseline Model

The vehicle dynamics can be found using the Lagrange equations of motion. In this approach, the total kinetic energy and potential energy of the vehicle are derived and are placed into the equations of motion. Additional details are described in the work by Gilbert [46]. Equation 1 provides examples of the generalized force formulations used in the paper by Waszak and Schmidt [38]. This paper outlines a model tailored for for the B-1 swept wing bomber in the subsonic, incompressible flight regime. Additional details on the performance of this model were given in the paper by Schmidt and Rainey in 2001 [47]. Between these two papers the model was generated with the B-1 bomber parameters for the sake of validation.

$$\begin{aligned} \frac{d}{dt}\frac{\partial T}{\partial v_0} &= F \\ \frac{d}{dt}\frac{\partial T}{\partial \omega} + v_0\frac{\partial T}{\partial v_0} + \omega^x\frac{\partial T}{\partial \omega} &= M \\ \frac{d}{dt}\frac{\partial T}{\partial \dot{q}} - \frac{\partial T}{\partial q} + \frac{\partial v}{\partial q} &= Q \end{aligned} \tag{1}$$

Lagrange energy equations for vehicle equations of motion

Figures 3 and 4 show the vehicle's pitching response for a rigid model and a flexible model based on the work in [38]. Figure 3 shows the same maximum pitch rate excursions as well as the same settling pitch rate as given in the paper by Schmidt and

Rainey. Figure 4 shows the same maneuver with the 4 wing aeroelastic modes included in the dynamic model as described in Waszak and Schmidt [38].

Figures 5 and 6 are the magnitude and phase plots for the B-1 model in response to a chirp input that swept from 0.1 Hz up to 15 Hz. Figure 5 is the rigid model and figure 6 is the aeroelastic model. The details for how the magnitude and phase plots were obtained for the original publication is not clear, though the most likely was a linearization of the dynamic model and an analytical formulation of the transfer function for pitch rate. In figures 5 and 6, the frequency response was obtained by generating a sweeping input to the control surface and performing the input-output correlation analysis on the time history of this data. The important parts to note is the correlation to the peak at 1 rad/sec for the phugoid mode as see in the original publication. Figure 6 also exhibits the same peak in the phase plot at values above 200 rad/sec, indicating the same structural mode resonance published in Waszak and Schmidt.

Aerodynamic modeling may be achieved in a variety of ways. Generally, steady aerodynamic models are acceptable for most aircraft designs where the structure may be considered semi rigid. Under such formulations, the aerodynamic model for a surface with an airfoil 2-D cross-section may be described as given in equation 2. In this case, the coefficient C_{l_α} is constant and the alpha term is solely depended on the vehicle state with respect to the local wind vector.

$$L = \frac{1}{2} \rho V^2 S C_{l_\alpha} \alpha * l_{char} \tag{2}$$

A slightly more advanced model, as explained in the paper by Waszak and Schmidt, now takes approximations of the sectional properties that include the shape of the bending mode Φ and the bending mode's current state vector, $[\eta ; \dot{\eta}]$. Changes in angle of incidence i and wing sweep profile are also considered in this aerodynamic model given in equation 3.

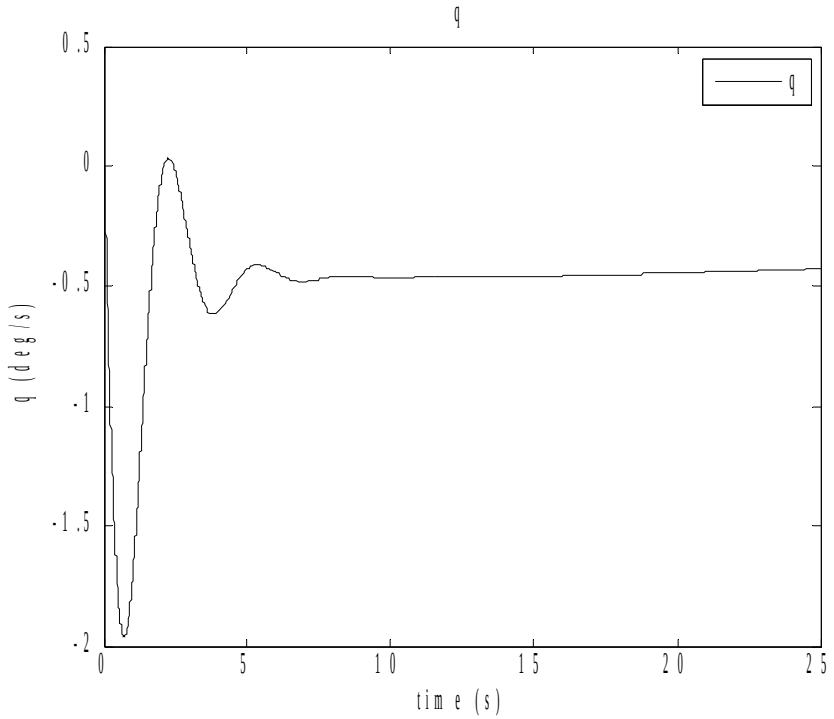

Figure 3: Step response for rigid B-1 model

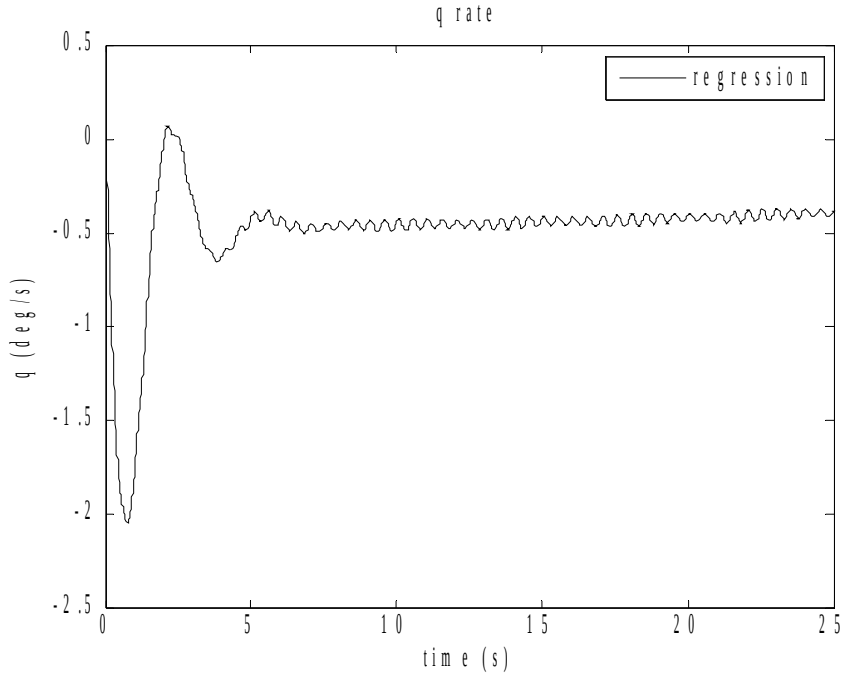

Figure 4: Step response for flexible B-1 model

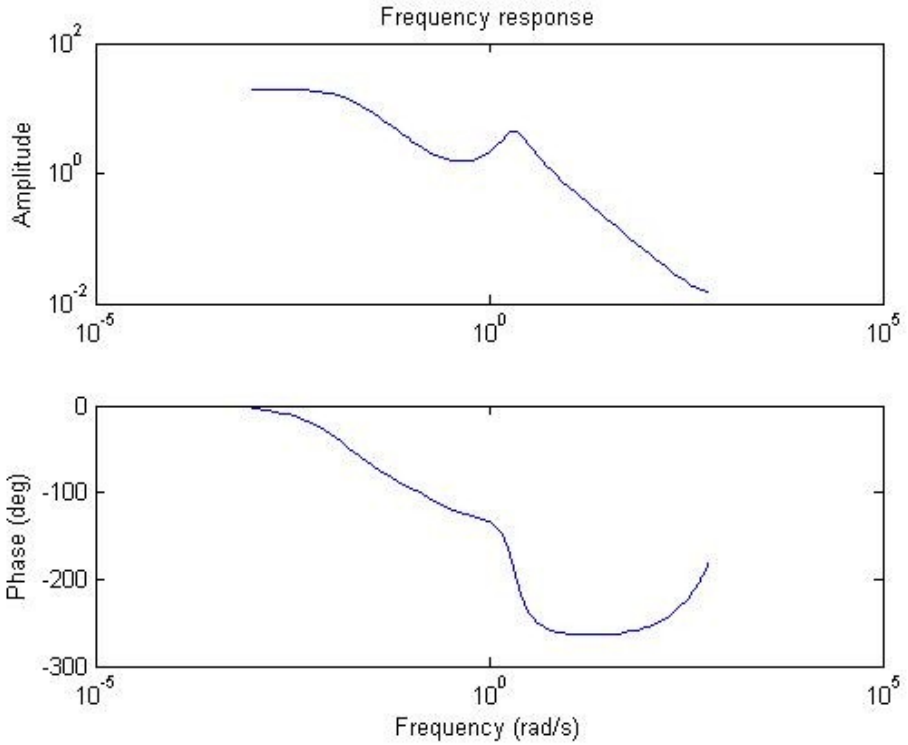

Figure 5. Magnitude and phase plot for rigid B-1 model

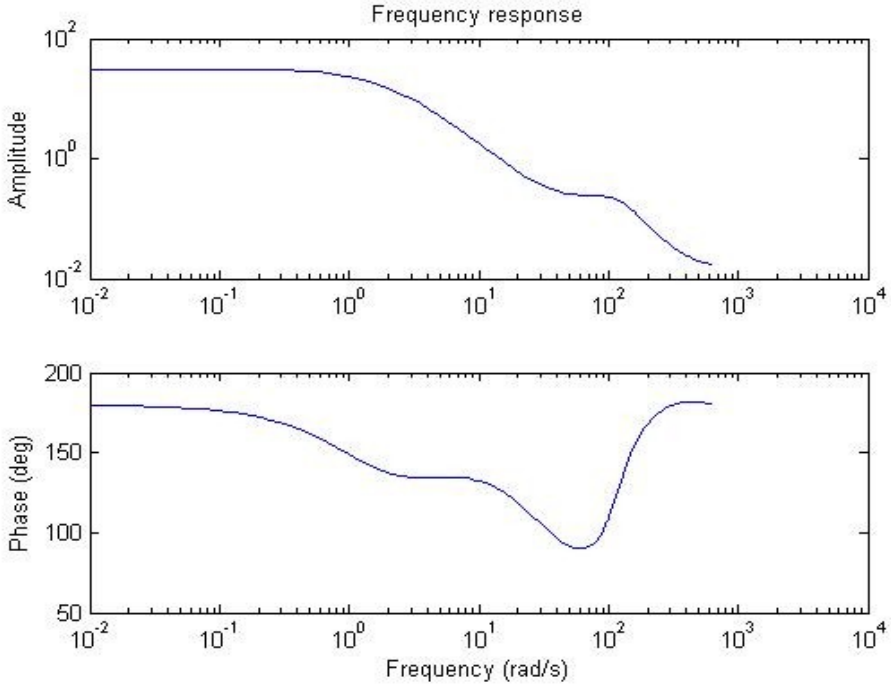

Figure 6: Magnitude and Phase plot for flexible B-1 model

$$\alpha_s = \alpha_v + i_s - q\left(\frac{\Delta x + e}{U}\right) + p\frac{y}{U} + \sum_{i=1}^{\infty}\left[\left(\frac{d\phi_i^b}{dx}\right)\eta_i + \frac{1}{U}\phi_i^b\dot{\eta}_i\right] \tag{3}$$

The most sophisticated aerodynamic models used before the davent of computational fluid dynamics (CFD) consider fully unsteady flow, meaning the aerodynamics of the vehicle are time dependent and not necessarily periodic. Turbulence and other characteristics can be modeled using these techniques. There are a variety of approaches to modeling unsteady aerodynamics and they become particularly interesting in the area of aeroelasticity. One of the more widely accepted models is the Peters unsteady aerodynamic model [48] which is what is employed in the NATASHA code discussed later in this paper. The most attractive property of the Peters model is that it may be configured as a state-space model [49] making it a convenient alternative for flight dynamic models. The full name of the model is the finite-state unsteady thin-airfoil theory. This model includes both the free stream flow behavior and includes the induced flow from the shed vorticity of the unsteady flow field.

For a one-to-one comparison to the models above, the angle of attack equation for the Peters model is given in equation 4. This angle of attack is based of the expected value at the 3-quarter wing chord of an arbitrary lifting volume. The variable h accounts for the plunging motion of the wing and λ_0 represents vorticity. Each λ is an inflow state. The total inflow can thus be represented as a superimposed series of these states at different strengths, locations and position. The combined effect provides a description of the flow of air in the volume of interest that is unsteady with time.

$$\alpha = \theta + \frac{\dot{h}}{U} + \frac{b}{U}\left(\frac{1}{2} - a\right)\dot{\theta} - \frac{\lambda_0}{U} \tag{4}$$

$$\text{Where} \quad \lambda_0 \approx \frac{1}{2}\sum_{n=1}^{N} b_n \lambda_n$$

The state-space representation is realized by expanding the inflow model and defining the variable A as follows:

$$[A]\dot{\lambda}+\frac{U}{b}\lambda=c\left[\ddot{h}+U\dot{\theta}+b\left(\frac{1}{2}-a\right)\right] \tag{5}$$

$$[A]=[D]+\{d\}\{b\}^T+\{c\}\{d\}^T+\frac{1}{2}\{c\}\{b\}^T \tag{6}$$

Finally, the parameters for D, b, d, and c are defined using a few simple series approximations:

$$D_{nm}=\begin{cases}\frac{1}{2n}, & n=m+1\\ -\frac{1}{2n}, & n=m-1\\ 0, & n\neq m\pm 1\end{cases} \qquad b_n=\begin{cases}(-1)^{n-1}\frac{(N+n-1)!}{(N-n-1)!}\frac{1}{(n!)^2} & n\neq N\\ (-1)^{n-1}, & n=N\end{cases} \tag{7a}$$

$$d_n=\begin{cases}\frac{1}{2}, & n=1\\ 0, & n\neq 1\end{cases} \qquad c_n=\frac{2}{n} \tag{7b}$$

Figure 7 demonstrates the effect of adding additional inflow states to the aerodynamic model by Peters. The input here was 5 ft/s velocity for a wing section idealized by being connected to a base by springs and dampers. There is a point were additional states do not provide added information and eventually, too many states will make the model unstable as shown by the plot for 17 inflow states in figure 6.

A model of the apparent mass effects can also be included as has previously been done for parafoils [50]. As noted by Slegers [50] , Barrows [51] and Lissaman [52], parafoils and straight wing added mass effects can be modeled as approximate ellipsoids. There are limits on the effectiveness of this model for larger aspect ratios. Equation set 8 summarizes these terms for mass and second moments of inertia.

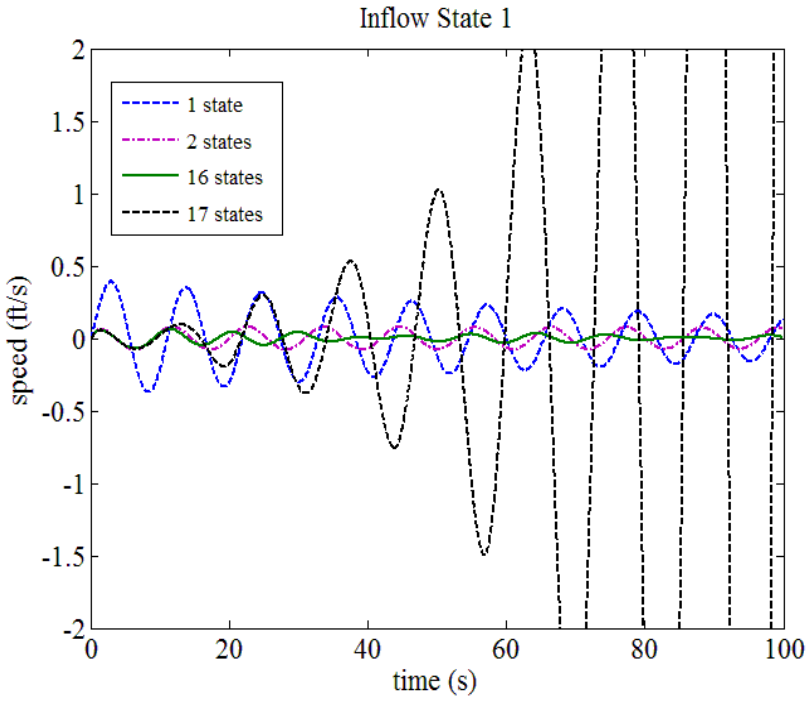

Figure **7:** Variation of inflow state 1 with increased inflow state modeling

$$
\begin{aligned}
m_{f11} &= k_A \pi (t^2 b/4) & I_{f11} &= 0.055 \left[\frac{AR}{(1+AR)} \right] b\, S^2 \\
m_{f22} &= k_B\, pi\, (t^2 c/4) & I_{f22} &= 0.0308 \left[\frac{AR}{(1+AR)} \right] c^3 S \\
m_{f33} &= \left[\frac{AR}{(1+AR)} \right] \pi (c^2 b/4) & I_{f33} &= 0.055\, b^3 t^2
\end{aligned}
\tag{8}
$$

These added mass and added inertia terms are then used in the mass matrix used to describe the full 6 degree-of-freedom equations for vehicle motion.

$$
\mathbf{M} = \begin{bmatrix} m\mathbf{I} & -m\,\mathbf{r}^x \\ m\,\mathbf{r}^x & \mathbf{J} \end{bmatrix} + \begin{bmatrix} \mathbf{m}_{added} & 0 \\ 0 & \mathbf{J}_{added} \end{bmatrix} \tag{9}
$$

$$
\mathbf{m}_{added} = \begin{bmatrix} m_{f11} & 0 & 0 \\ 0 & m_{f22} & 0 \\ 0 & 0 & m_{f33} \end{bmatrix} \quad \mathbf{J}_{added} = \begin{bmatrix} I_{f11} & 0 & 0 \\ 0 & I_{f22} & 0 \\ 0 & 0 & I_{f33} \end{bmatrix}
$$

$\mathbf{r}^x$ = skew-symmetric matrix of position vector of the center of mass from the origin
$\mathbf{I}$ = Identity matrix

3.2 Flight Dynamics

3.2.1 Short Period Approximation

Based off the equations used by Waszak and Schmidt, the longitudinal motion of the aircraft is described by:

$$\dot{q} = \frac{(-I_{xz}^2 + I_{xx} I_{zz})(Q_{theB} + (-I_{xx} + I_{zz})\, pr - I_{xz}(p^2 - r^2))}{-I_{xz}^2 I_{yy} + I_{xx} I_{yy} I_{zz}} \tag{10}$$

$$\dot{U} = \frac{Q_x}{M} + rV - qW - g\sin\theta \tag{11}$$

$$\dot{W} = \frac{Q_z}{M} + qU - pV + g\cos\theta\cos\phi \tag{12}$$

The equations are simplified by removing any terms not relevant to longitudinal motion and factoring out $(-I_{xz}^2 + I_{xx} I_{zz})$ from the $\dot{q}$ equation yielding:

$$\dot{q} = \frac{Q_{theB}}{I_{yy}} \tag{13}$$

$$\dot{U} = \frac{Q_x}{M} - qW - g\sin\theta \tag{14}$$

$$\dot{W} = \frac{Q_z}{M} + qU + g\cos\theta \tag{15}$$

The small perturbation formulation assumes disturbances of the the form:

$$\alpha = \alpha_o + \Delta\alpha \ , \ \ etc. \tag{16}$$

For speeds, the small disturbance takes the form of:

$$u=\frac{\Delta U}{U_0},\quad w=\frac{\Delta w}{U_0} \tag{17}$$

The equation for $\dot{q}, \dot{U},$ and $\dot{W}$ then become:

$$\Delta C_{Q_x}=\frac{m U_0}{\frac{1}{2}\rho U_0^2 S}\dot{U}=\frac{2\mathrm{m}}{\rho U_0 S}\dot{U} \tag{18}$$

$$\Delta C_{Q_Z}=\frac{2m}{\rho U_0 S}(\Delta\dot{\alpha}-q) \tag{19}$$

$$\Delta C_{Q_q}=\frac{I_{yy}}{\rho U_0^2 S\bar{c}}\dot{q} \tag{20}$$

Here, the right hand side has terms left over from the non-dimensionalization of the all the terms in the above equations. The left-hand side of these equations may than be substituted by the generalized loads formulated in the Lagrange equations Starting with the equations for the dimensionalized Lagrange forces, the nondimensional forms of the equations are found.

$$\begin{aligned}Q_\theta=&\frac{\rho V_0^2 S}{2}\left(C_{Mo}+C_{\theta\alpha}\alpha+C_{M\delta}\delta+\sum_{i=1}^{\infty}C_{M\eta_i}\eta_i\right)\\&+\frac{\rho V_{oS}\bar{c}}{4}\left(C_{M\dot{\alpha}}\dot{\alpha}+C_{Mq}q+\sum_{i=1}^{\infty}C_{M\dot{\eta}}\dot{\eta}_i\right)+T_M\end{aligned}$$

$$\begin{aligned}Q_Z=&\frac{\rho V_0^2 S}{2}\left(C_{Zo}+C_{Z\alpha}\alpha+C_{Z_\delta}\delta+\sum_{i=1}^{\infty}C_{Z_{\eta_i}}\eta_i\right)\\&+\frac{\rho V_{oS}\bar{c}}{4}\left(C_{Z_{\dot{\alpha}}}\dot{\alpha}+C_{Z_q}q+\sum_{i=1}^{\infty}C_{Z_{\dot{\eta}_i}}\dot{\eta}_i\right)+T_Z\end{aligned} \tag{21}$$

$$\begin{aligned}Q_{\eta_j}=&\frac{\rho V_0^2 S}{2}\left(C_0^{\eta_j}+C_\alpha^{\eta_j}\alpha+C_\beta^{\eta_j}\beta+C_\delta^{\eta_j}\delta+\sum_{i=1}^{\infty}C_{\eta_i}^{\eta_j}\eta_i\right)\\&+\frac{\rho V_{oS}\bar{c}}{4}\left(C_{\dot{\alpha}}^{\eta_j}\dot{\alpha}+C_p^{\eta_j}p+C_q^{\eta_j}q+C_r^{\eta_j}r+\sum_{i=1}^{\infty}C_{\dot{\eta}_i}^{\eta_j}\dot{\eta}_i\right)\end{aligned}$$

The generalized loads are nondimensionalized as follows:

$$\begin{aligned} C_{Q_X} &= \left(C_{X_0} + C_{X\alpha}\Delta\alpha + C_{X\delta}\Delta\delta + C_{X\eta}\Delta\eta\right) \\ &\frac{+\bar{c}}{2}\left(C_{X\dot{\alpha}}\Delta\dot{\alpha} + C_{Xq}\Delta q + C_{X\dot{\eta}}\Delta\dot{\eta}\right) + C_{Tx}\Delta\delta_T \end{aligned}$$

$$\begin{aligned} C_{Q_Z} &= \left(C_{Z_0} + C_{Z\alpha}\Delta\alpha + C_{Z\delta}\Delta\delta + C_{Z\eta}\Delta\eta\right) \\ &\frac{+\bar{c}}{2}\left(C_{Z\dot{\alpha}}\Delta\dot{\alpha} + C_{Zq}\Delta q + C_{Z\dot{\eta}}\Delta\dot{\eta}\right) + C_{Tz}\Delta\delta_T \end{aligned} \tag{22}$$

$$\begin{aligned} C_{Q\theta} &= \bar{c}\left(C_{M_0} + C_{M\alpha}\Delta\alpha + C_{M\delta}\Delta\delta + C_{M\eta}\Delta\eta\right) \\ &\frac{+\bar{c}^2}{2}\left(C_{M\dot{\alpha}}\Delta\dot{\alpha} + C_{Mq}\Delta q + C_{M\dot{\eta}}\Delta\dot{\eta}\right) + C_{MT}\Delta\delta_T \end{aligned}$$

Because this is the short period approximation, any formulation relating to the vehicle speed is not of interest. As a result, the equation for U and ΔC_{Q_X} are eliminated. In there place is the equation for the wing bending mode:

$$\ddot{\eta}_i + \omega_i^2\eta = \frac{Q_{\eta i}}{M_i} \tag{23}$$

where, the solution for these sets of equations take the form of a series of sinusoidal functions as is general knowledge after a class on ordinary differential equations (ODEs).

$$\eta_i = F_i\sin(\omega_i t) \quad \text{or} \tag{24}$$

$$\eta_i = G_i\cos(\omega_i t)$$

At this point, the generalized force for the wing bending modes may be added to the equation. Including the effects for only the first bending mode, the equation takes the form of:

$$\begin{aligned} \ddot{\eta}_1 + \omega_1^2\eta_1 = \frac{1}{N_1}&\left(C_0^{\eta_1} + C_\alpha^{\eta_1}\Delta\alpha + C_\delta^{\eta_1}\Delta\delta + C_{\eta_1}^{\eta_1}\Delta\eta_1\right) \\ &+ \frac{\bar{c}}{2}\left(C_{\dot{\alpha}}^{\eta_1} + C_q^{\eta_1}\Delta q + C_{\dot{\eta}}^{\eta_1}\Delta\dot{\eta}_1\right) \end{aligned} \tag{25}$$

Performing the Laplace transforms and dividing all three equations by the elevator input gives a form of each equation which fits nicely into matrix form to solve for the different transfer functions of interest.

As an example, the result of these operations are shown below for the wing bending equation:

$$\left(s^2+\omega_1^2-C_{\eta_1}^{\eta_1}k_1-c_1 s C_{\eta_1}^{\eta_1}\right)\frac{\Delta\eta_1(s)}{\Delta\delta(s)}-\left(c_1 C_{\dot{\alpha}}^{\eta_1}s+k_1 C_{\alpha}^{\eta_1}\right)\frac{\Delta\alpha(s)}{\Delta\delta(s)}-(c_1 C_q^{\eta_1}s\frac{\Delta\theta(s)}{\Delta\delta(s)})=C_{\delta}^{\eta_1} \tag{26}$$

Next, the three equations may be solved simultaneously in matrix form:

$$\begin{bmatrix}(s I_{yl}-c_1 C_{mq})s & -(C_{m\alpha}+c_1 C_{m\dot{\alpha}}s) & -(C_{m\eta}+c_1 C_m\dot{\eta}_1 s)\\ s(m_1-c_1 C_{mq})s & (m_1 s-c_1 C_{Z\dot{\alpha}}s-C_Z\alpha) & -(C_{Z\eta_1}+c_1 C_Z\dot{\eta}_1 s)\\ -(c_1 C_q^{\eta_1}s) & -(c_1 C_{\dot{\alpha}}^{\eta_1}s+k_1 C_{\alpha}^{\eta_1}) & (s^2+\omega_1^2-C_{\eta_1}^{\eta_1}k_1-c_1 s C_{\dot{\eta}_1}^{\eta_1})\end{bmatrix}\begin{bmatrix}\frac{\Delta\theta(s)}{\Delta\delta_e(s)}\\ \frac{\Delta\alpha(s)}{\Delta\delta_e(s)}\\ \frac{\Delta\eta(s)}{\Delta\delta_e(s)}\end{bmatrix}=\begin{bmatrix}C_{m\delta}\\ C_{Z\delta}\\ C_{\delta}^{\eta_1}\end{bmatrix} \tag{27}$$

Using Cramer's rule, the transfer function for the θ Euler angle is found.

$$\frac{\Delta\theta(s)}{\Delta\delta_e(s)}=\frac{\begin{vmatrix}C_{m\delta} & -(C_{m\alpha}+c_1 C_{m\dot{\alpha}}s) & -(C_{m\eta_1}+c_1 C_{m\dot{\eta}_1}s)\\ C_{Z\delta} & (m_1 s-c_1 C_{Z\dot{\alpha}}s-C_{Z\alpha}) & -(C_{Z\eta_1}+c_1 C_{Z\dot{\eta}_1}s)\\ C_{\delta}^{\eta_1} & -(c_1 C_{\dot{\alpha}}^{\eta_1}s+k_1 C_{\alpha}^{\eta_1}) & (s^2+\omega_1{}^2-C_{\eta_1}^{\eta_1}k_1-c_1 s C_{\dot{\eta}_1}^{\eta_1})\end{vmatrix}}{\begin{vmatrix}(s I_{yl}-c_1 C_{mq})s & -(C_{m\alpha}+c_1 C_{m\dot{\alpha}}s) & -(C_{m\eta}+c_1 C_m\dot{\eta}_1 s)\\ s(m_1-c_1 C_{mq})s & (m_1 s-c_1 C_{Z\dot{\alpha}}s-C_Z\alpha) & -(C_{Z\eta_1}+c_1 C_Z\dot{\eta}_1 s)\\ -(c_1 C_q^{\eta_1}s) & -(c_1 C_{\dot{\alpha}}^{\eta_1}s+k_1 C_{\alpha}^{\eta_1}) & (s^2+\omega_1^2-C_{\eta_1}^{\eta_1}k_1-c_1 s C_{\dot{\eta}_1}^{\eta_1})\end{vmatrix}} \tag{28}$$

Carrying out the determinants yields the transfer functions:

$$\frac{\Delta\theta(s)}{\Delta\delta(s)}=$$

$$(-C_{\alpha}^{\eta_1}k_1-c_1C_{\alpha}^{\eta_1}s)(-C_{m\eta_1}C_{Z\delta}-c_1C_{m\dot{\eta}}C_{Z\delta}s-c_1C_{m\delta}C_{Z\delta}s-c_1C_{m\delta}C_{Z\dot{\eta}}s)+$$
$$(-C_{m\delta}C_{Z\alpha}-C_{m\alpha}C_{Z\delta}-c_1C_{m\delta}C_{Z\dot{\alpha}}sc_1C_{m\dot{\alpha}}C_{Z\delta}s+C_{m\delta}m_1s)(-C_{\eta_1}^{\eta_1}k_1+\omega_1^2-c_1C_{\dot{\eta}_1}^{\eta_1}s+s^2)+$$
$$C_{\eta_1\delta}((C_{m\alpha}+c_1C_{m\dot{\alpha}}s)(-C_{Z\dot{\eta}}s-c_1C_{Z\dot{\eta}}s)-(C_{m\eta}+c_1C_{m\dot{\eta}s})(-C_{Z\dot{\alpha}}s+m_1s))$$

$$((-C_{\alpha}^{\eta_1}k_1-c_1C_{\dot{\alpha}}^{\eta_1}s)(-(-c_1C_{Zq}+m_1)s(C_{m\eta_1}+c_1C_{m\dot{\eta}_1}s)$$
$$+s(-C_{Z\eta_1}-c_1C_{z\dot{\eta}_1}s)(-c_1C_{mq}+I_{yI}s))$$
$$-c_1C_q^{\eta_1}s((C_{m\alpha}+c_1C_{m\dot{\alpha}}s)(-C_{Z\eta_1}-c_1C_{Z\dot{\eta}_1}s)-(C_{m\eta_1}+c_1C_{m\dot{\eta}_1}s)(-C_{Z\alpha}-c_1C_{Z\dot{\alpha}}s+m_1s))$$
$$+(-C_{\eta_1}^{\eta_1}k_1+\omega_1^2-c_1C_{\dot{\eta}_1}^{\eta_1}s+s^2)$$
$$(-(-c_1C_{Zq}+m_1)s(C_{m\alpha}+c_1C_{m\dot{\alpha}}s+s(-c_1C_{mq}+I_{yI}s)(-C_z\alpha-c_1C_{Z\dot{\alpha}}s+m_1s))))$$

(29)

The transfer function for the theta angle is a power of s 3 over 6 relationship and therefore, the pitch rate transfer function is a power of s 4 over 6 relationship. This is the model for a single bending mode. If additional bending modes are deemed of importance, their influence may be added in a similar fashion.

3.2.2 Dihedral Effect

Based on equation 3, the importance of the local angle of attack on a wing section is evident. As will be noted in chapter 4 on the experimental setup, the most successful glider design during testing included built-in dihedral. This dihedral will effect the local angle of attack and thus the quasi-steady contribution of the wing's aerodynamics during a turn. Though this portion of flight what not analyzed in the model matching component of the results, the effect is still noted as follows.

The glider uses a rudder and elevator control scheme. To turn, a rudder input causes the plane to yaw and the dihedral effect induces a rolling moment allowing the platform to make a controlled turn. Based on the text by Etkin [24], a yawed wing will produce a differential in angle of attack between the upwind half of the wing and the downwind half. This effect is proportional to the vertical and lateral components of the

wind frame velocity vector. For small angles, an approximation may be made as shown below.

$$V_n = w\cos\Gamma + v\sin\Gamma \qquad (30)$$
$$V_n = w + v\Gamma$$

3.3 NATASHA Model

The wing was modeled as a half-span cantilevered beam. The stiffness matrix is given as:

$$\begin{Bmatrix}\epsilon\\ \kappa\end{Bmatrix} = \begin{bmatrix}R & S\\ S^T & T\end{bmatrix}\begin{Bmatrix}\boldsymbol{F}\\ \boldsymbol{M}\end{Bmatrix} \qquad (31)$$

This equation is detailed by Raghavan for a beam or wing with a completely uncoupled stiffness matrix. This is often a reasonable baseline approximation:

$$\begin{Bmatrix}\epsilon_1\\ \epsilon_2\\ \epsilon_3\\ \kappa_1\\ \kappa_2\\ \kappa_3\end{Bmatrix} = \begin{bmatrix}1/(EA) & 0 & 0 & 0 & 0 & 0\\ 0 & 1/(k_2GA) & 0 & 0 & 0 & 0\\ 0 & 0 & 1/(k_3GA) & 0 & 0 & 0\\ 0 & 0 & 0 & 1/(GJ) & 0 & 0\\ 0 & 0 & 0 & 0 & 1/(EI_2) & 0\\ 0 & 0 & 0 & 0 & 0 & 1/(EI_3)\end{bmatrix}\begin{Bmatrix}F_1\\ F_2\\ F_3\\ M_1\\ M_2\\ M_3\end{Bmatrix} \qquad (32)$$

To populate this equation, information is needed on the bending, torsional and axial stress and strain properties of the wing. The parameters are found experimentally or by analytical approximation. I_2 and I_3, the area moments of inertia for a given wing segment are found with the formula derived for a beam:

$$I_y = c\frac{\Delta b^3}{12} \qquad I_z = \frac{t/2\,c^3}{12} \qquad (33)$$

The other significant parameter determining the shape and frequency of the structural modes of the wing is the sectional mass. For an inflatable structure, the cross-section is

not isotropic between the air gap, the polyurethane membrane, and any supporting structures such as carbon fiber rods. In addition, the mass and inertial would need to account for the added mass and added inertia effects due to the low mass to volume ratio. Therefore, the section properties for most cases, must be treated as effective values and not representative of what is actually seen in any one component that makes up the wing cross-section, figure 8.

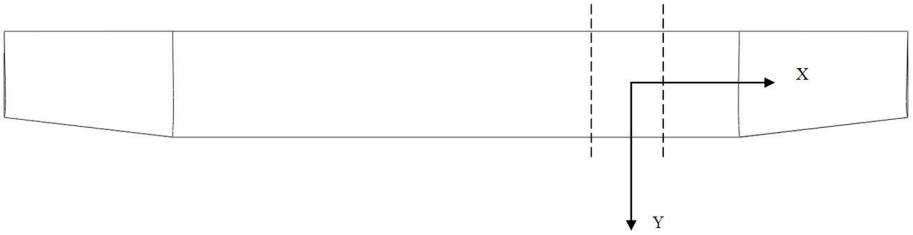

Figure 8: Wing cross-section

Aerodynamic loading on the wing during flight is simplified for the purpose of approximating the structural loads on the wing surface. A lift distribution close to the elliptic distribution shown in figure 9 is assume and the loads can then be simplified as shown in figure 10.

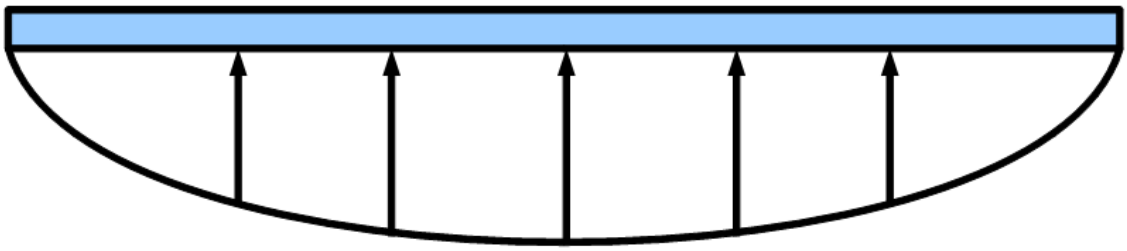

Figure 9: Elliptic Lift Distribution

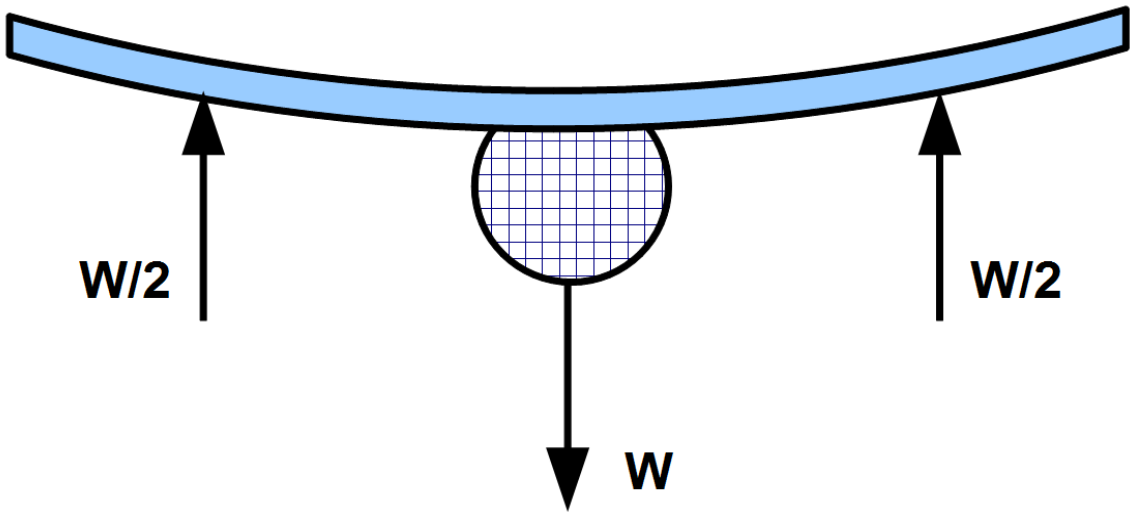

Figure 10: Loads idealization

The Elastic modulus is approximated from basic beam bending theory by considering the setup shown in figure 11. Equation 34 shows the relationship between tip deflection of the beam, or wing in this case, and the loading and length of the bean or wing. The same can be done for the axial and torsional properties by considering other loading cases such as that shown in figure 12.

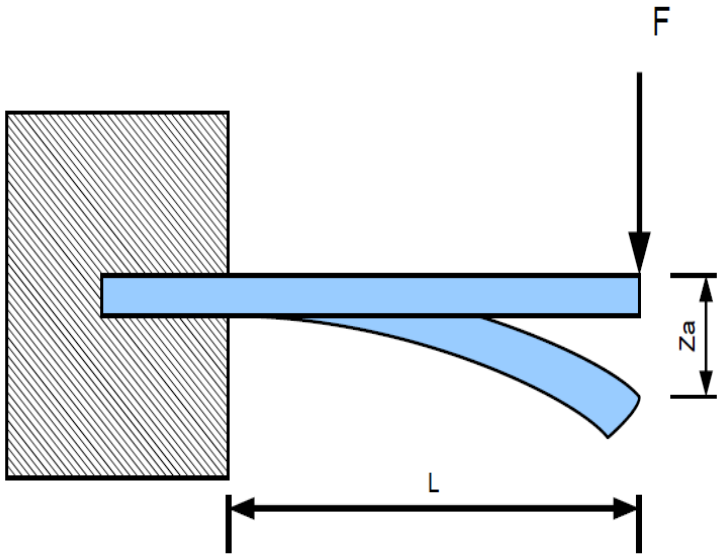

Figure 11: Cantilevered beam simplification

$$z_A = \frac{-F L^3}{3 E I} \tag{34}$$

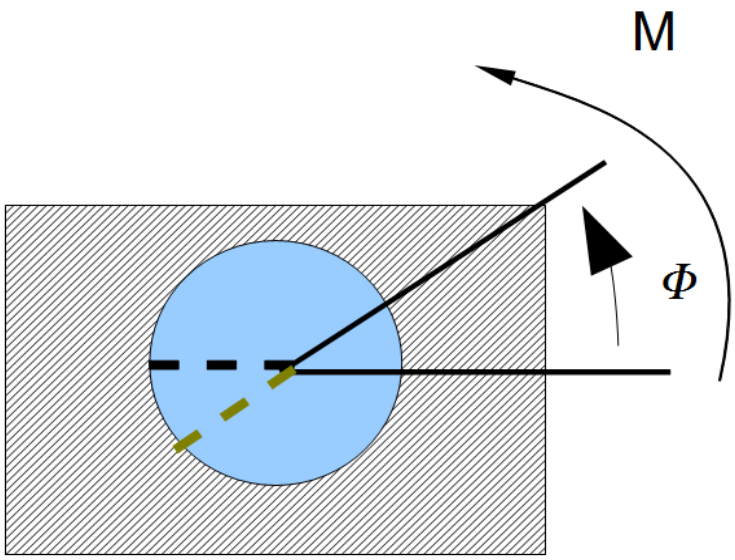

Figure 12: Torsional load idealization

A similar estimation may be made about the torsional rigidity of the beam. This approximation is assumed valid until the onset of wrinkling, at which point, the relationship between input moments and linear or angular deflections would not be consistent with previous results. Due to the inherently low shear modulus of the thermoplastic polyurethane membrane used here, this onset of wrinkling may be seen very early. However, the cross-sectional mechanics of materials properties of the wing will be very different from those of the membrane on its own (4 mils). This is even more so the case with a carbon fiber reinforced wing which will show visible signs of wrinkling on the surface of the membrane, while still far from the failure point of the overall cross-section shape.

As a result, in the end, the material properties of the polyurethane membrane are not of any consequence for this analysis. For the analysis in NATASHA to be useful, some experimental numbers must be obtained that describe the behavior of each wing as a whole. Each case will differ enough due to the variability in the number of supporting carbon fiber rods utilized in each case as described in chapter 5.

CHAPTER 4

EXPERIMENTAL SETUP

The integrity of the process of acquiring test flight data is important in understanding the significance of the results obtained. Chapter 4 details the process in reaching a final vehicle design and what software and hardware was chosen to capture data and what some anticipated benefits or downfalls may be associated with the choices described.

4.1 Modifying an Existing Platform

The majority of work during the experimental phase consisted of flight testing to acquire telemetry useful to validate models and parametrize the longitudinal flight mode. To begin with, a platform had to be chosen that would be suitable for flight testing. This lead to a glider kit platform to take advantage of some basic qualities such as the low take-off weight and increased glide ratio as compared to other configurations.

The initial plan was to mount the inflatable wing to an existing kit and capture flight test data from this configuration. An Aspire EP electric glider kit was readily available, and after flight testing the unmodified kit, it appeared that the platform would make an acceptable option. The total weight of the platform was found in order to estimate expected static deflection of the inflatable wing under loads comparable to the total launch weight of the glider. A simple pull test with a harness was conducted. Figures 13 and 14 show the wing's configuration under testing. The results from the initial pull test in table 4.1 show that the wing sustained expected loads under moderate static deflection. The stiffening carbon rods were secured with tape compatible with the thermoplastic polyurethane so the supports could be reconfigured easily. The wing was

initially mounted to the body with rubber bands with a wing harness to allow the wing to hold well to the balsa wood frame. This harness was eventually also abandoned.

Figure 13: Wing supports

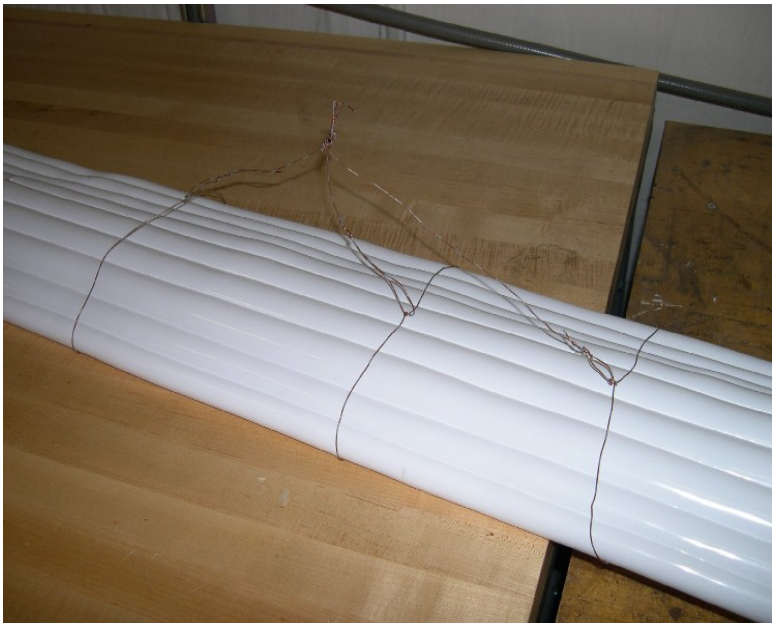

Figure 14: Pull Test Set up

Table 4.1 Wing tip deflections

Number of support rods	Measured pull weight	Tip deflection
0	1.52 lbs	16 1/8 inches
1	1.48 lbs	10 inches
2	1.52 lbs	5 5/8 inches

Figures 15 and 16 show frequency response plots for the Aspire EP platform with a conventional wing. This data was collected as a proof of concept for the system identification process that was eventually used, as discussed in the results section. The frequency response was obtained for the two transfer functions of primary interest in the longitudinal vehicle dynamics. This information was obtained using CIFER (Comprehensive Identification from Frequency Responses). This software, developed by the Army's UARC (University Affiliated Research Center), in northern California performs the frequency analysis of time history data. Thought a process that used Fourier transforms, it determines the magnitude and phase of the vehicle's state response to control inputs over a specified frequency range. The main result from this step in the experimental setup is the correlation between the input and output frequency decompositions. This characteristic is given a weighting known as the coherence between the two signals. CIFER scales coherence between 0 and 1, where values above 0.6 are considered indicators of acceptable correlation. Looking at the coherence plot at the bottom of both the q/δ_e and the θ/δ_e , it can be seen that high correlation was captured by the autopilot/ data-logger withing the range of expected piloted commands (1 – 12 rad/sec). The range of the phase plot is also a good sign of the control bandwidth of the vehicle in this range. Though the eventual platform was different from the Aspire EP, this

initial step was useful as a validation of much of the hardware and software that was eventually used.

The layout of the hardware and software interface is given in figure 17.

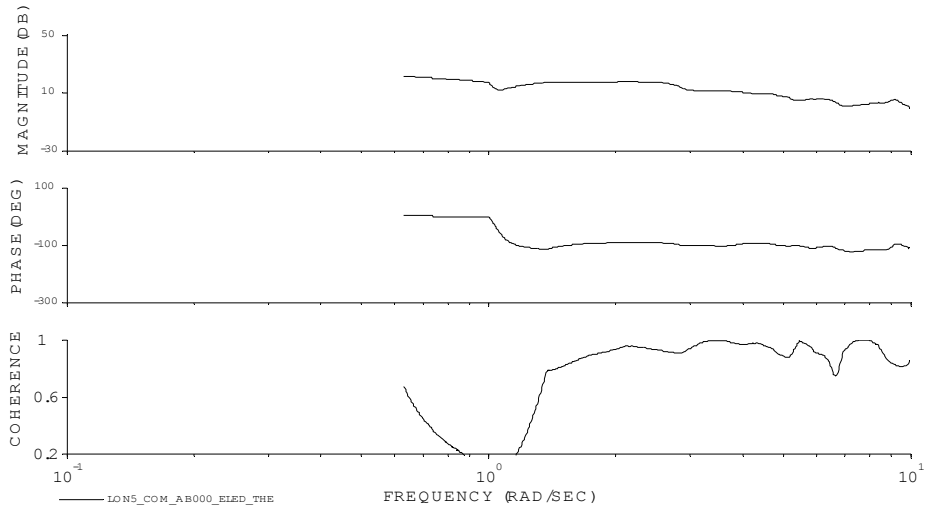

Figure 15: Frequency response of the elevator to θ bare airframe dynamics

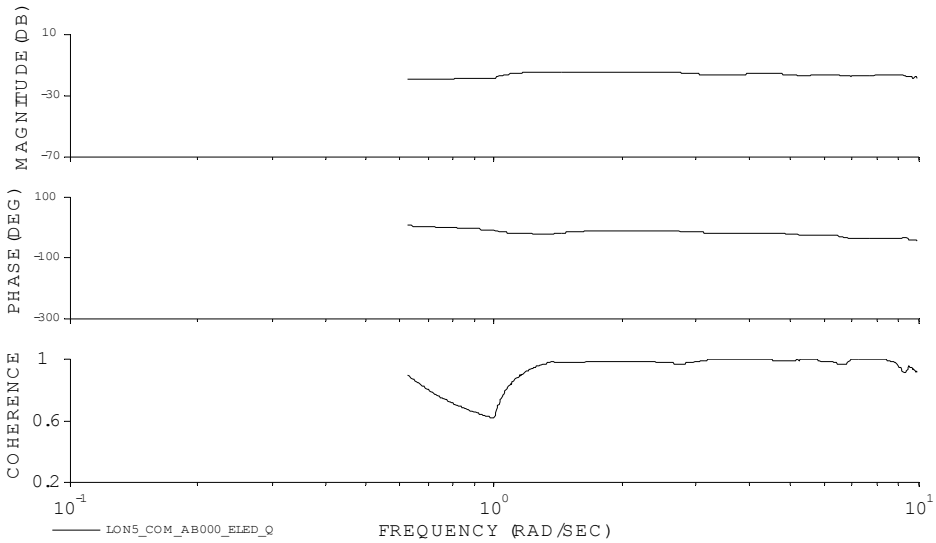

Figure 16: Frequency response of the elevator to pitch rate bare airframe dynamics

The Eltima RS-232 data logging software provides a simplified user interface allowing the user to capture serial data from any port on the computer in real time. It handles file concatenation and all the settings normally associated with serial data logging such as baud rate and parity bits. The 2.4 GHz Xbee receiver allows wireless communication with the autopilot at half a watt of power output. Depending on the need for GPS, data is transferred at different rates and the settings of the data-logger may need to be adjusted according.

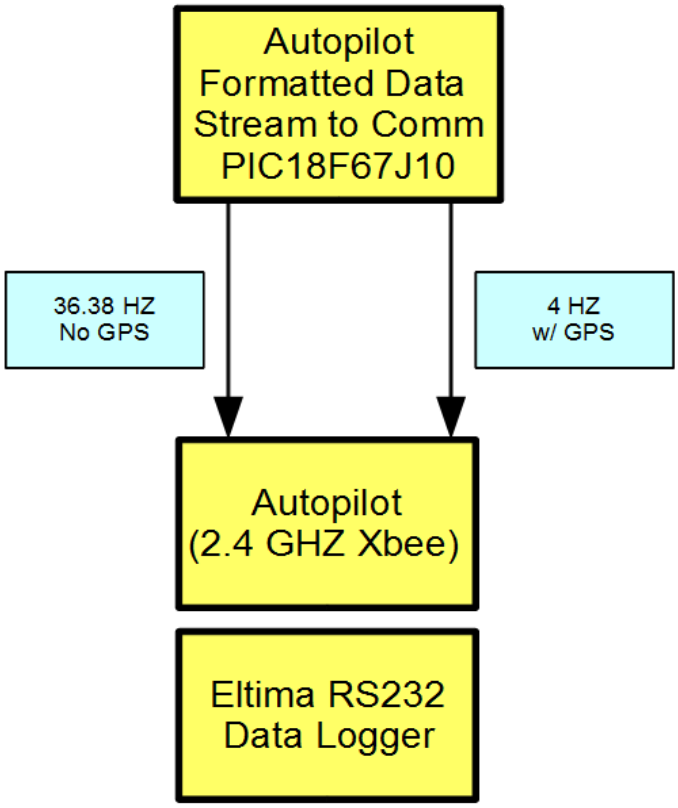

Figure 17: Data-logging diagram

4.2 Foam EP

After some difficulty with the weight and layout of the Aspire EP's frame, it was decided to move to a more accommodating platform in the form of a foam replica. This would provide a much needed weigh reduction as well as a custom shaped frame that would provide a less obtrusive pocket for the inflatable wing to sit in. The easy to work with EPP foam would also allow easy and quick modifications and prototyping to make needed improvements to the balance and trim of the aircraft's control mechanisms (propeller, elevator and rudder as well as angle of incidence of the vertical and horizontal tail and propeller). Figures 18 and 19 show the resultant platform used for the flight testing discussed in the results section in chapter 5.

Figure 18: Experimental platform

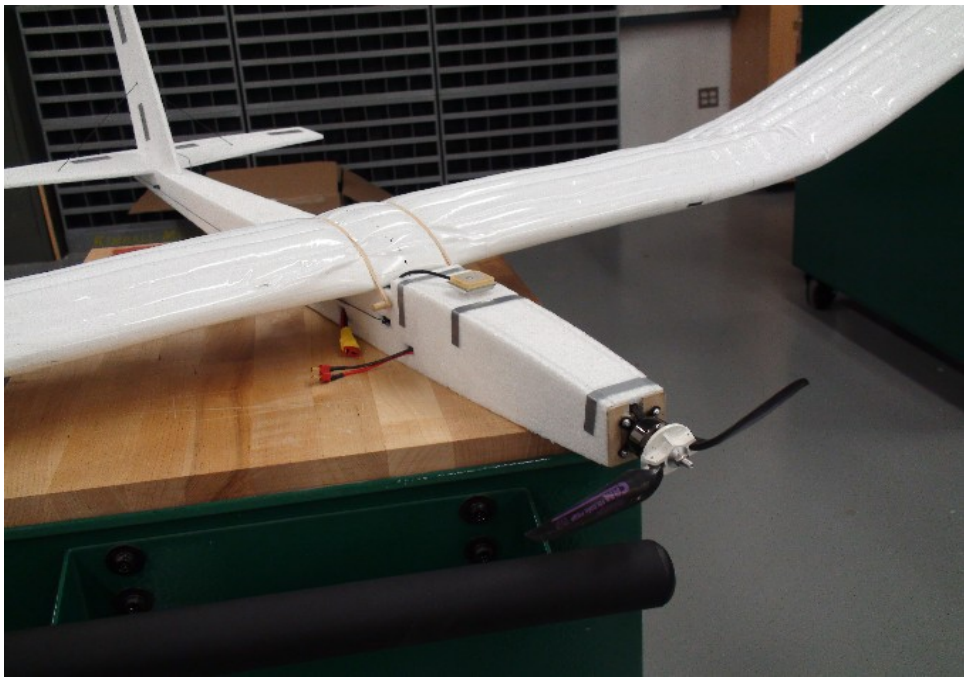

Figure 19: Experimental Platform propeller and wing mounting detail

To make a working estimate of the glider's moment of inertia tensor, a replica of the platform was designed in Solidworks, which is a CAD software package. All the major internal components, such as batteries and motors were modeled to their measured weight and geometry. The frame's composite density was approximated by matching the weight of the overall assembly to the weight of the glider measured from a lab scale. Figure 20 provides a rendering of the model that was used. Appendix B figure B.1 contains the 3 view drawing of the glider as well.

Though the primary purpose of the flight testing was to acquire input and output data of the vehicle's pitching motion, additional parameters used in the simulation model and relevant to the basic characterization of the glider where also of interest. Figures 21 to 23 show the lift-curve slope approximation as well as the flight velocity approximation of the glider during flight testing. Reiterating equation 2:

$$L_A = \frac{1}{2}\rho V_A^2 S C_{l_\alpha} \alpha_A * l_{char}$$

$$L_B = \frac{1}{2}\rho V_B^2 S C_{l_\alpha} \alpha_B * l_{char}$$

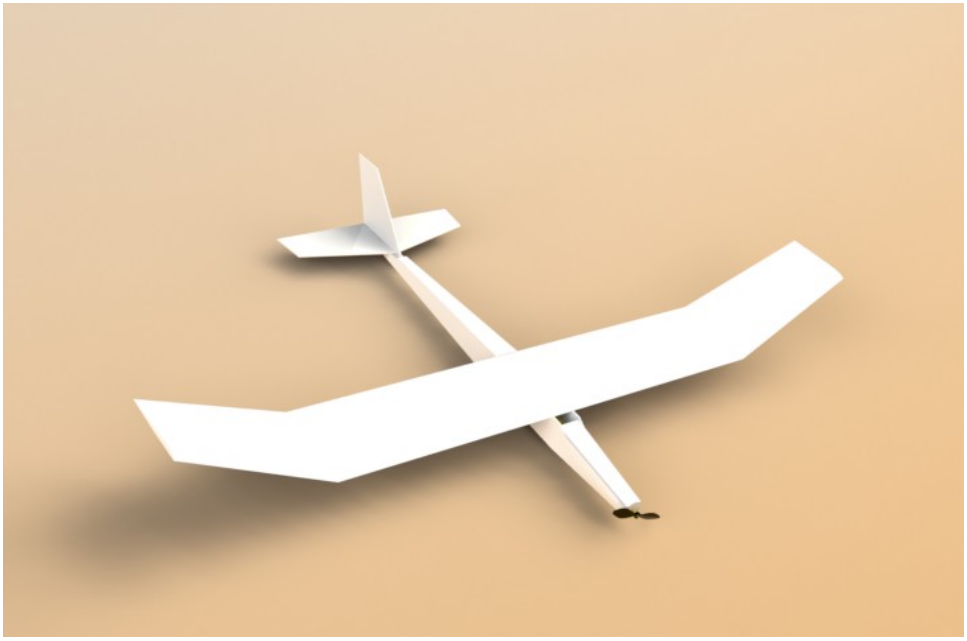

Figure 20: rendering of CAD model used for approximating mass model

In this case, the subscripts A and B simply refer to case A and B which represents different pieces of data for different trim conditions. By measuring the weight, the left side of each equation above is known for the equilibrium case. The angle of attack is known from the telemetry and the velocity is approximated from a combination of both GPS and accelerometer data. Figure 21 shows the linear approximation of the data taken at a few points where the data most reasonable. This requirement included regions where the vehicle was holding a constant speed with a steady angle of attack without turning.. The slope of the given line is then taken as $C_{l\alpha}$ and the intercept of the y-axis provides C_{L_0}. In spite of this, the data points are dispersed and the linear regression is only a best fit for the data points that were available.

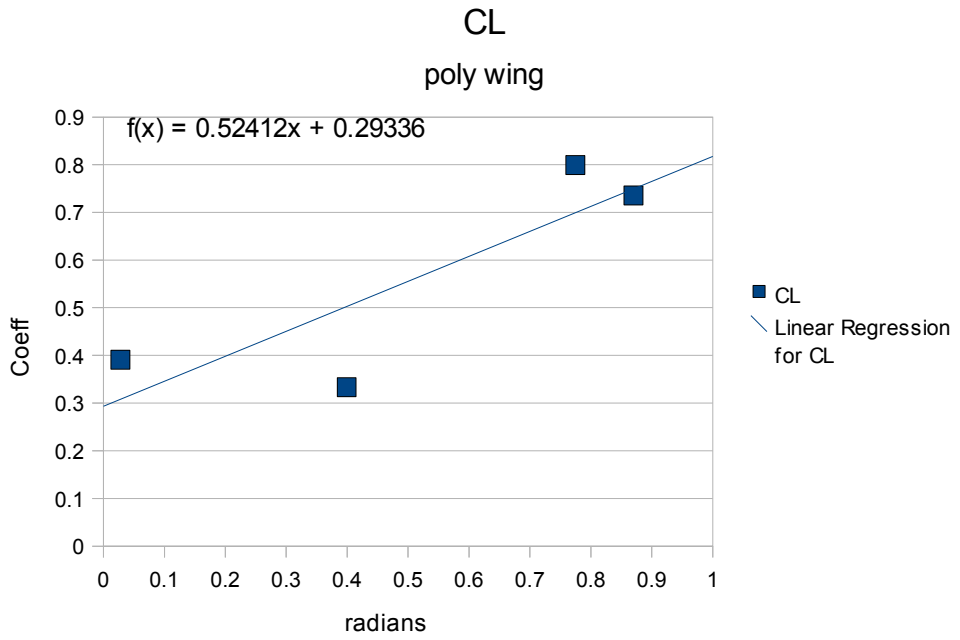

Figure 21: CL plot for Polyurethane wing

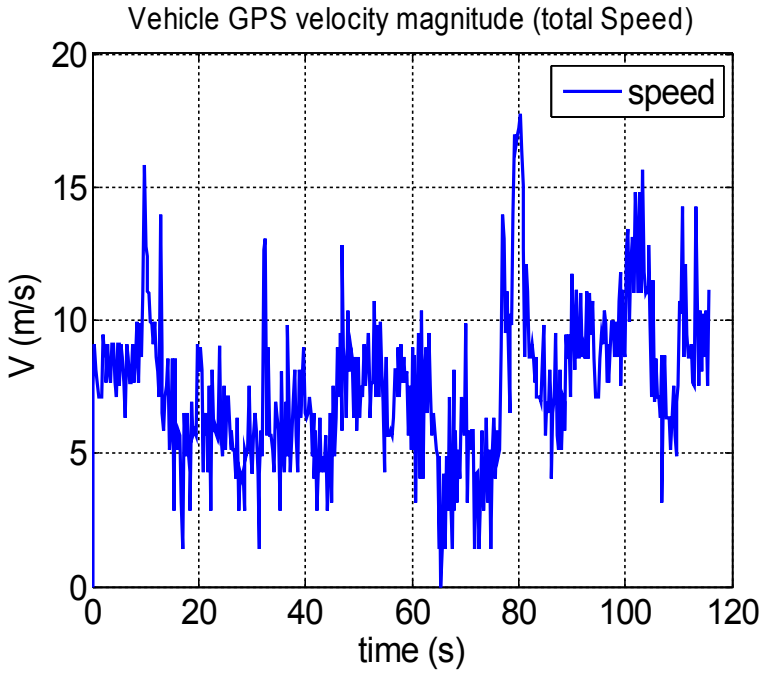

Figure 22: Example GPS total velocity plot for a given flight

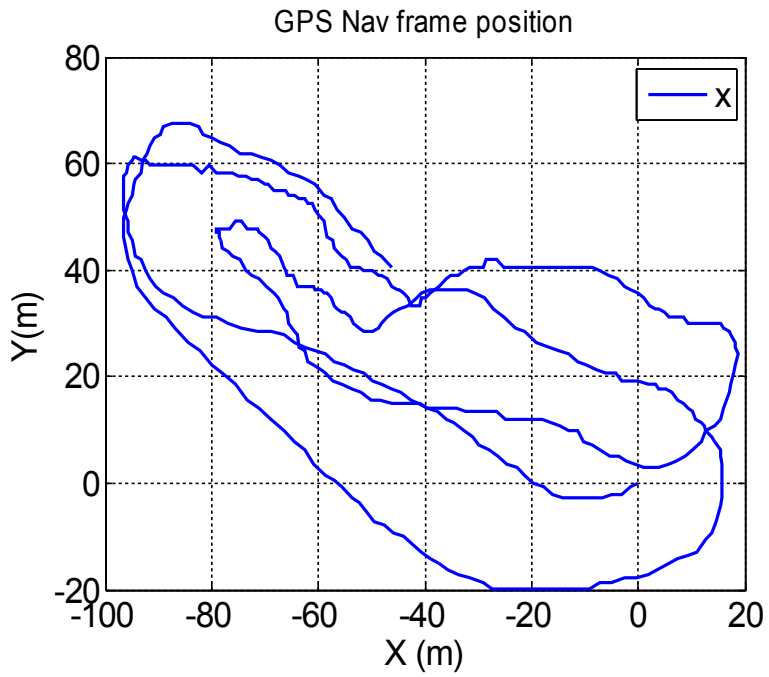

Figure 23: Example GPS plot of the glider's cross-range flight path

Eventually, testing focused on 2 main configurations. One configuration was a doubly supported polyurethane wing with dihedral to aid in lateral stability. The second configuration was a single carbon fiber rod supported wing which remained flat. This wing was the same wing used to test a completely free polyurethane configuration by simply removing the single support. This wing was also used to test an alternative configuration designed to improve the lack of directional controllability exhibited by the baseline design. Here, an 18 inch vertical fin as shown in figure 24 was attached over the wing and sized to provide similar turn capability as expected from the wing with dihedral. Both wings were also flown with helium for a comparison of the effect on increase added mass and added inertia. The weight of the first wing with dihedral was 315 grams with air and 302 grams with helium. The flat wing with a single support weighed 202 grams with air and 186 grams with helium. The weight of the dorsal fin was 29 grams.

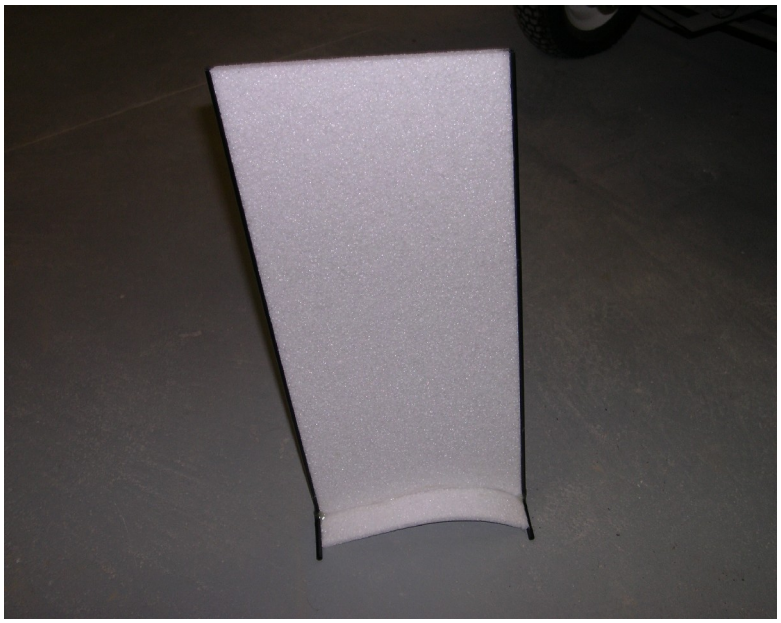

Figure 24: Dorsal fin for roll stability

4.3 Autopilot

The data capturing process involved the usage of the ARL Open-autopilot. The hardware and base software was developed as part of a collaboration between Professor Nathan Slegers of the University of Alabama, Huntsville and the Army Research Lab's Vehicle Technology Directorate. Since there is no official publication of this hardware and software, a short summary follows. The autopilot runs the majority of its code in C using Microchip PIC 8-bit microcontrollers. The functionality of these ICs are augmented by a Parallax Propeller chip to handle transmission of the PWM signals. The top board holds the main processing PIC chip and the Propeller chip. From figure 25, the 2.4 GHz Xbee radio is also visible. This network is the main communications link to the ground station laptop as outlined, previously in figure 17.

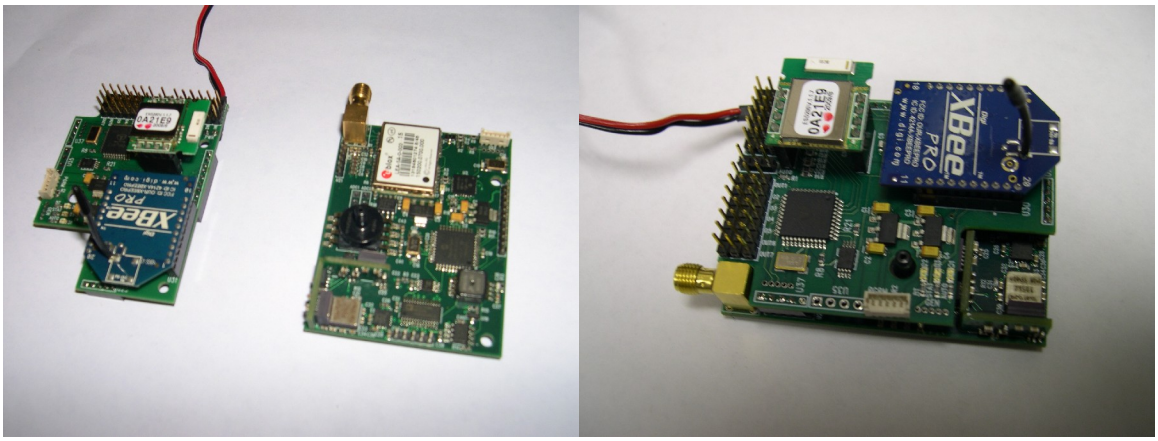

Figure.25: ARL/UAH Open Autopilot used to obtain results

The ground station includes data logger software from Eltima which records from any generic RS232 serial line. Connected to the ground station is a mated Xbee modem plugged into a USB adapter. Also on board the top half of the autopilot is a Bluetooth module that is not used for any portion of this testing. Up to seven servo channels may be read by the autopilot. For the purposes of the flight testing in this paper, only three channels were needed: throttle, elevator and rudder.

On the bottom board is the full sensor suite. This includes a $\mu-$blox 4 Hz GPS, 3 axis accelerometers, 3 axis gyroscopes, 3 axis magnetometers and a pitot tube perssure sensor and barometric altimeter. The raw data is run through a 16 channel ADC which converts the raw signal accordingly. The autopilot runs on 7.2 Volts.

With the experimental setup tested and validated, the experimental testing phase began to collect data to validate the simulation model.

CHAPTER 5

RESULTS

Successful results where obtained both from the analytical modeling section of the research as well as the experimental section. The following details what these results were and how their success is quantified.

5.1 Longitudinal Dynamics Model

The figures below show the experimental results for the glider's pitching angle with time against the output from the simulation model (Appendix A). In this model, the forces and moments are found for the vehicle by summing aerodynamics loads calculated with aerodynamic coefficients. The baseline values for the coefficients were found by the integral method explained by Gilbert [46]. and the code used is also included in Appendix A. The values of each coefficients were later tuned for each model. The wing bending is calculated at each time step by solving the sinusoidal function that describes the wing's motion. The state vector is simplified to include only the states of interested in a 3-degree-of-freedom longitudinal flight model. Thus, the states include $u, w, \theta, q, X, Y, \eta$. In the equations of motion, a more complicated expression is available for the pitch rate which includes the effect of added mass and inertia. The model was provided the same initial conditions as the test flight. The control model was fed a stream of deflections at the recorded update rate of the autopilot, which depended on the type of test. The model began to follow the simulation closely once approximations for several coefficients were inserted. Tables 5.1 to 5.3 below shows the values for the steady terms in the aerodynamic coefficient model.

Table 5.1: Z coefficients

C_{Z_0}	C_{Z_u}	C_{Z_w}	C_{Z_α}	C_{Z_q}	$C_{Z_{\delta_e}}$
-0.34	-10	-10.5	-15.51	14.7	-0.0076

Table 5.2: X coefficients

C_{X_0}	C_{X_u}	C_{X_w}	C_{X_α}	C_{X_q}	$C_{X_{\delta_e}}$
-0.028	0	-6.5	0.35	-1.7	0.00267

Table 5.3: Moment coefficients

C_{M_0}	C_{M_u}	C_{M_w}	C_{M_α}	C_{M_q}	$C_{M_{\delta_e}}$
4	0	0	0.005	-200	-0.55

With good steady state aerodynamic coefficients in place, it became an issue of adjusting the unsteady coefficients and the aeroelastic coefficients to match the flight test data as closely as possible. These parameters include:

$$C_{X_{\dot{\alpha}}},\ C_{X_{\eta_1}},\ C_{X_{\dot{\eta}_1}},\ C_{Z_{\dot{\alpha}}},\ C_{Z_{\eta_1}},\ C_{Z_{\dot{\eta}_1}},\ C_{M_{\dot{\alpha}}},\ C_{M_{\eta_1}},\ C_{M_{\dot{\eta}_1}} \tag{35}$$

The figures below show the performance of the model compared to the experimental data for the same control input. The first set of plots illustrate the response for the glider with the primary inflatable wing, which included dihedral at the wing tips and 2 support rods underneath. This was the design of the inflatable wing that deviated the farthest from the pure wing model, but was the most stable during test flight and still included visible signs of wing bending during flight.

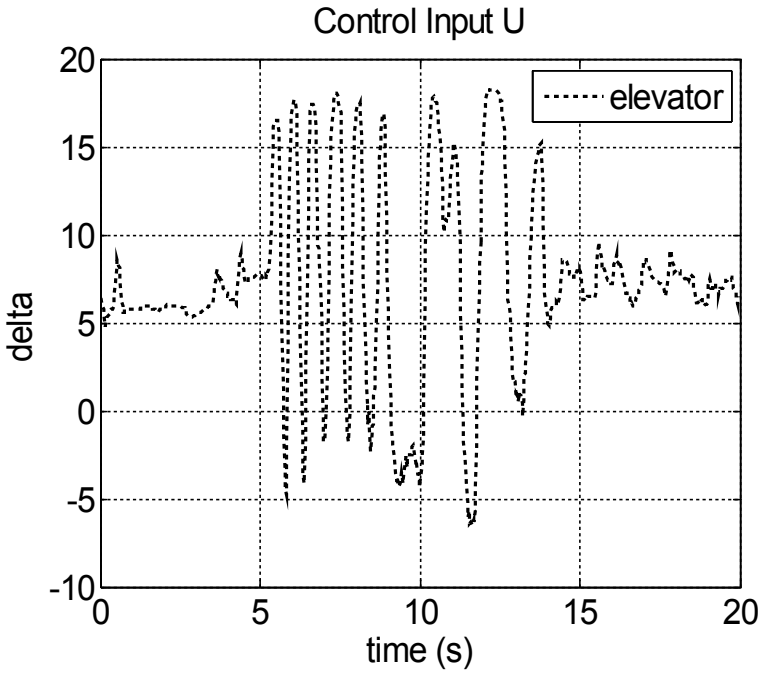

Figure 26: Control input to elevator

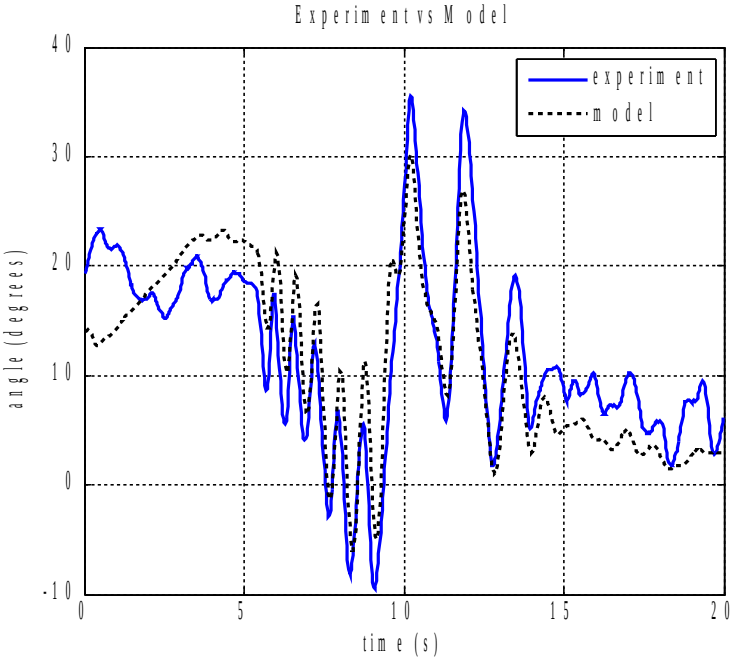

Figure 27: Theta for wing with supports

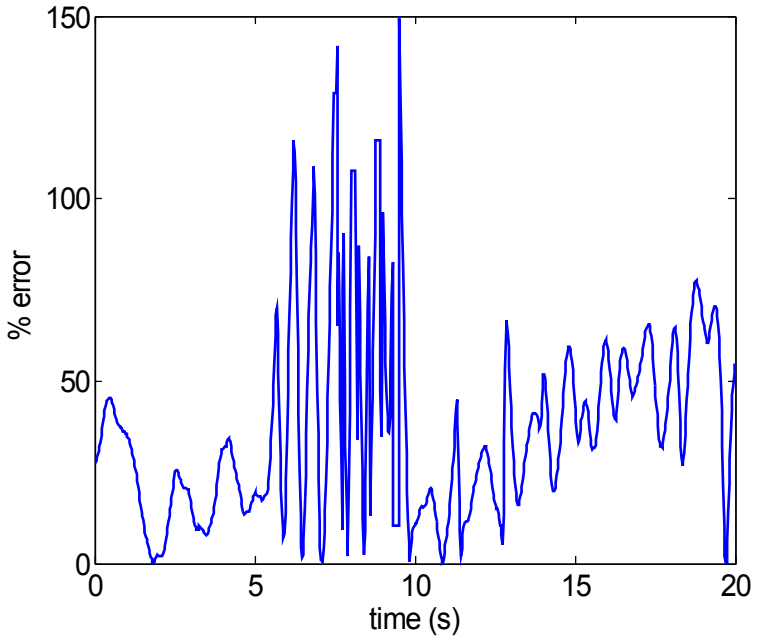

Figure 28: Error plot for wing with supports

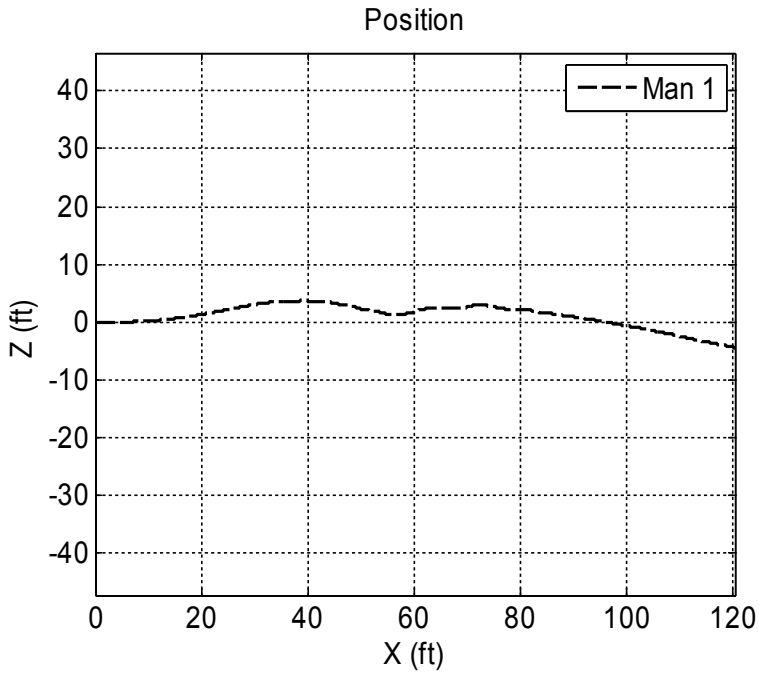

Figure 29: Simulation cross-range

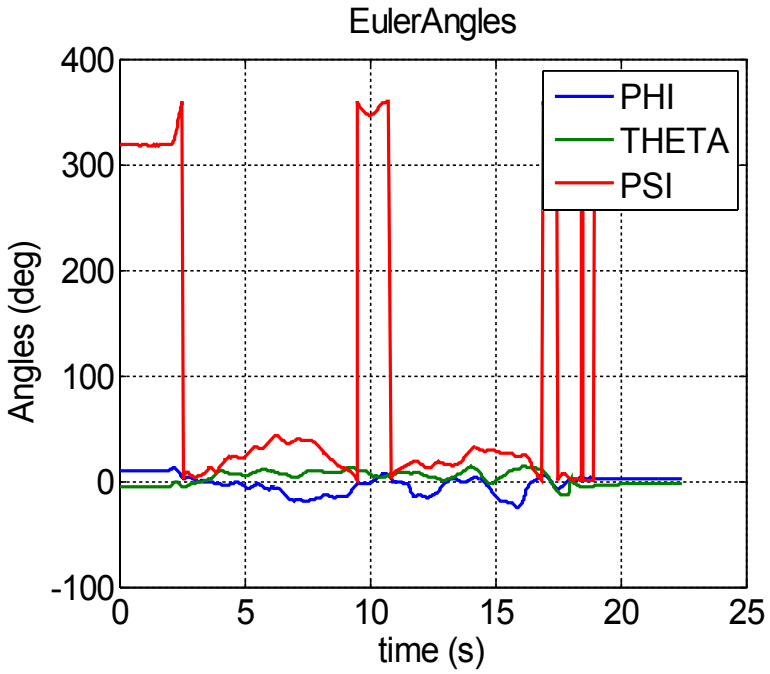

Figure 30: Euler angles for no supports

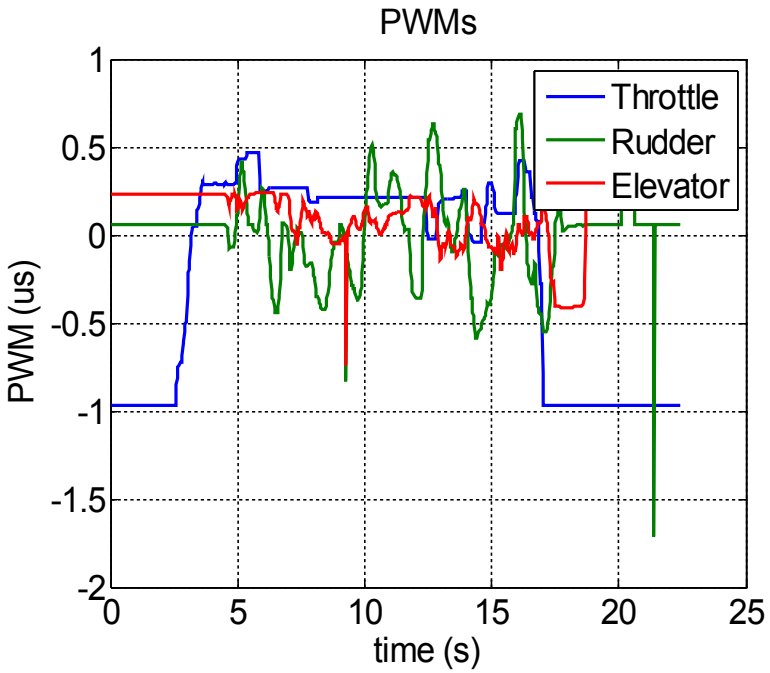

Figure 31: PWM for flight with no supports

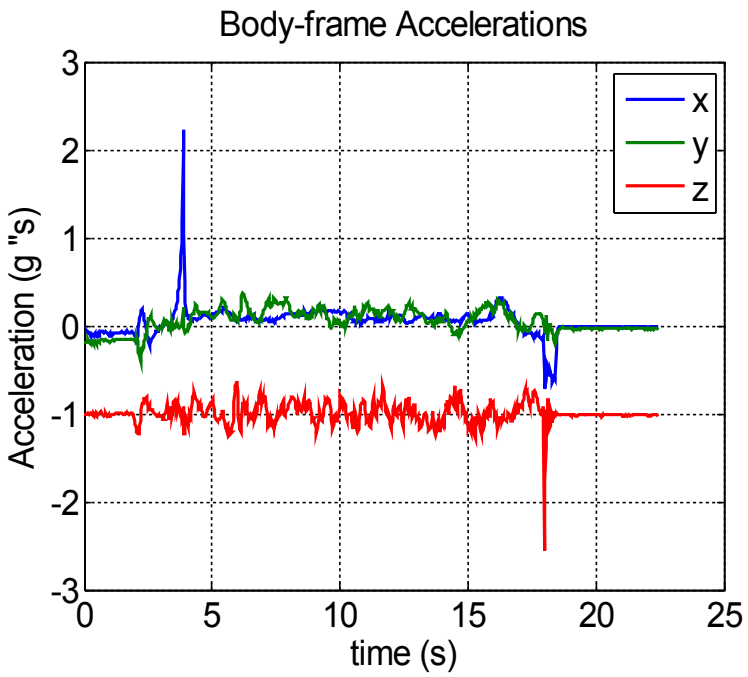

Figure 32: Accelerations for wing with no supports

The figures that follow (33-35) show the longitudinal response of the model and the experimental platform for the wing with no supports at all. This was without question the most unstable flight profile, especially in the presence of gust. While the winds calmed down, a straight ahead powered glide was performed with a discrete step input to provide some variation in the flight conditions along the powered glide maneuver. The plots below show the entirety of the flight profile.

This model was the most difficult to match. Part of the issue is the increased importance of the unsteady components of lift. Related to this is the increased sensitivity the platform exhibits towards wind gust. Figure 41 below shows the incremental effect of adding the first bending mode to the model. Because the the frequency of the bending mode is assumed, the result, as shown below is similar to a drift parameter over the duration of the flight. Figure 42 provides a more quantified explanation of the effect of the wing bending mode coefficients. By increasing $C_{M\eta}$, in this example, the average error over a given run of flight control inputs can be reduced for the more flexible models.

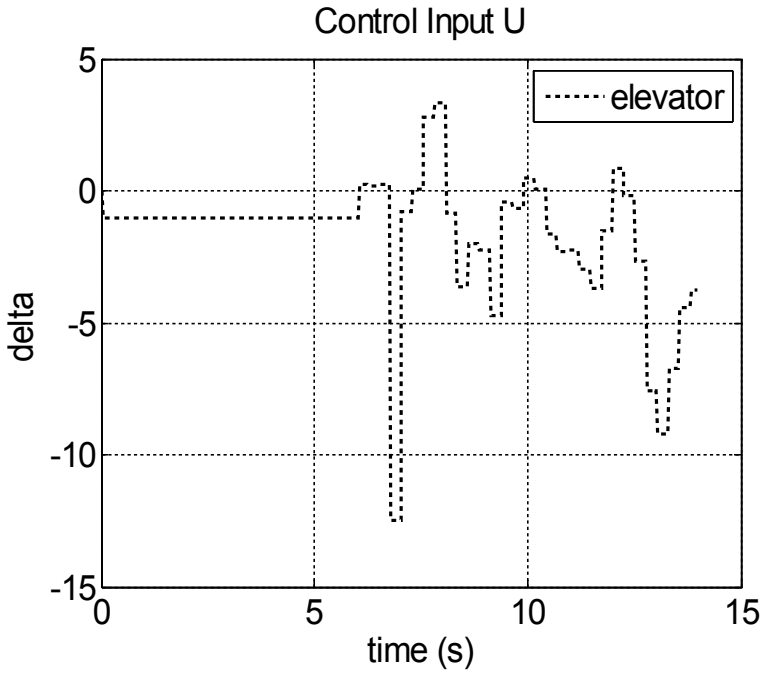

Figure 33: Control input for second case at 4 Hz

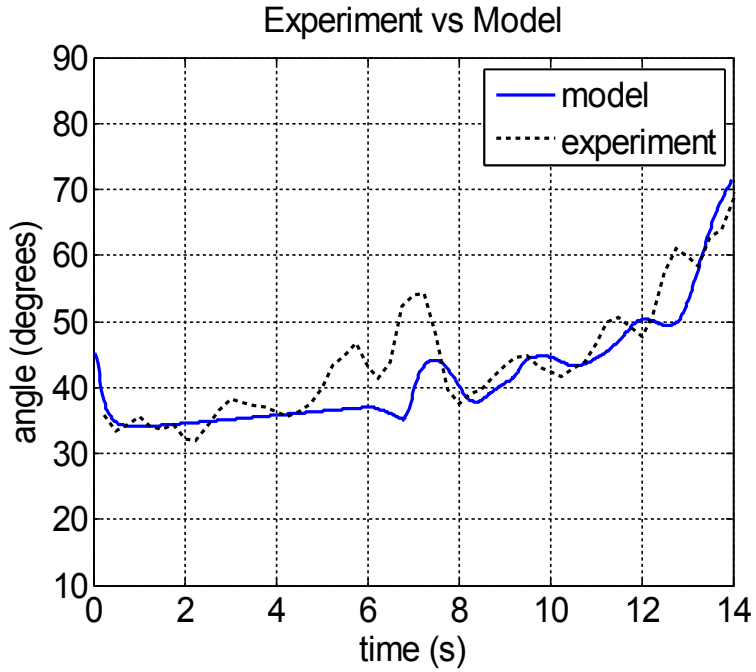

Figure 34: Theta for wing without supports

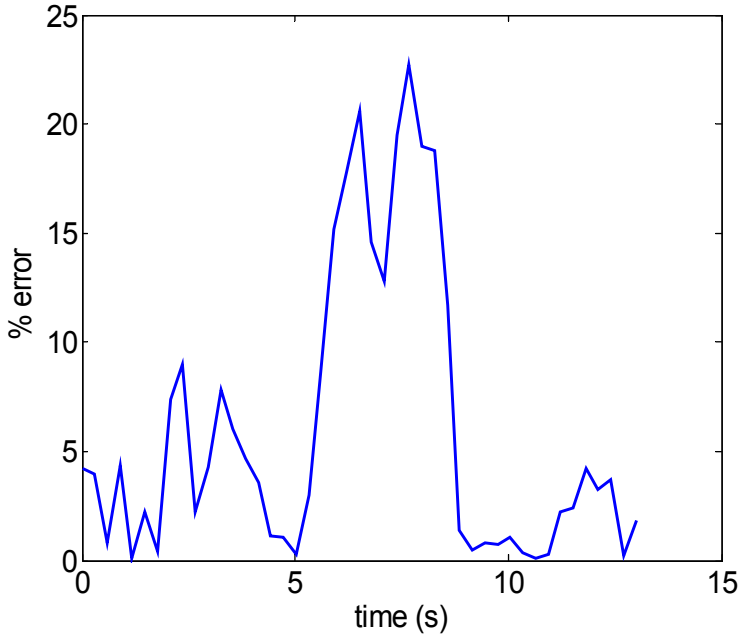

Figure 35: Error for theta for wing without supports

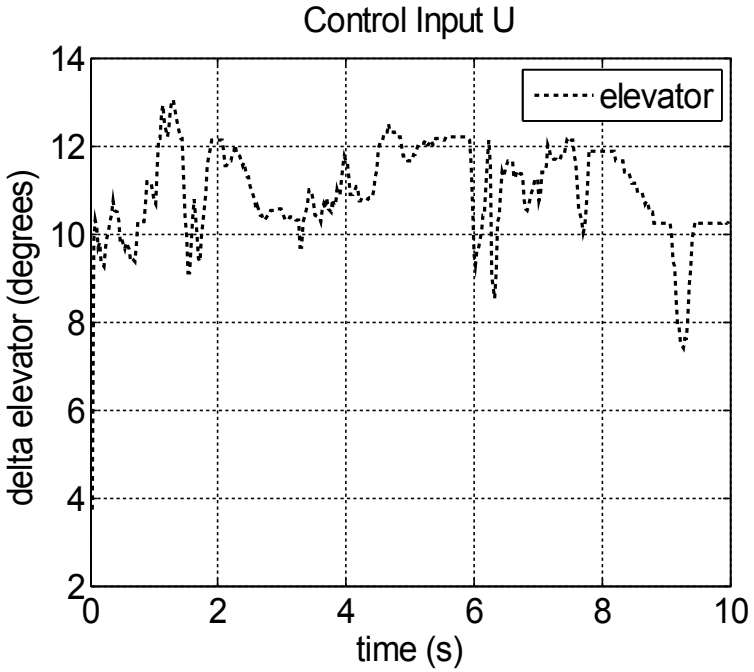

Figure 36: Rigid wing flight test elevator input

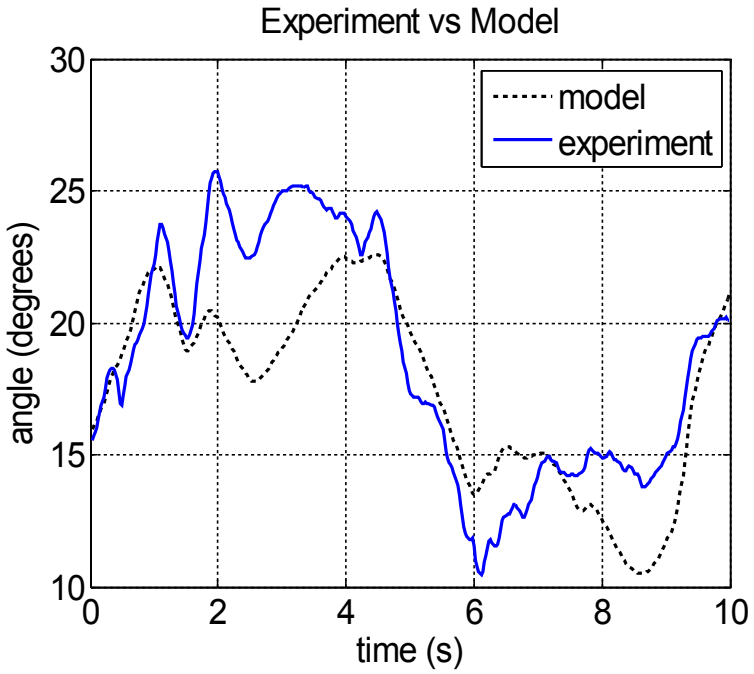

Figure 37: Rigid wing theta Euler angle response for flight test and simulation model

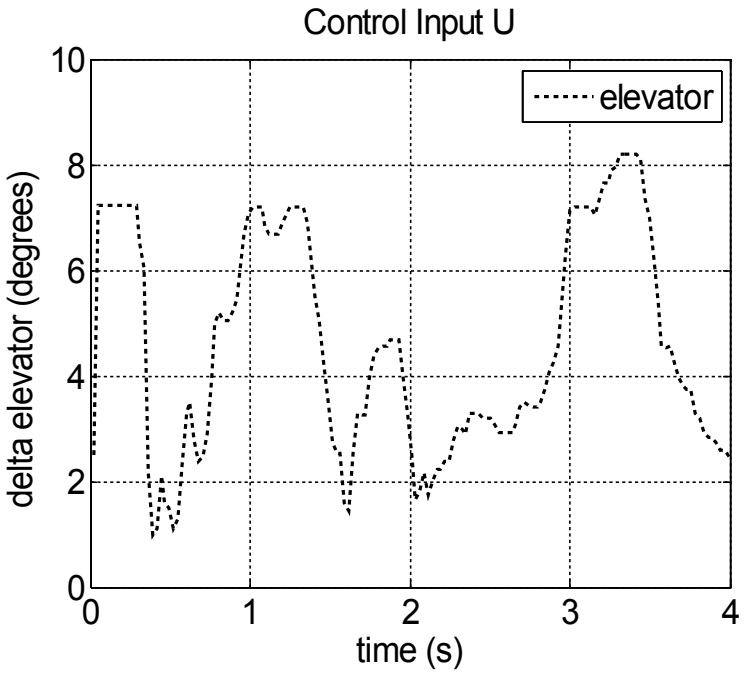

Figure 38: Flat wing elevator input with a single support inflated with helium and augmented with vertical fin before turn

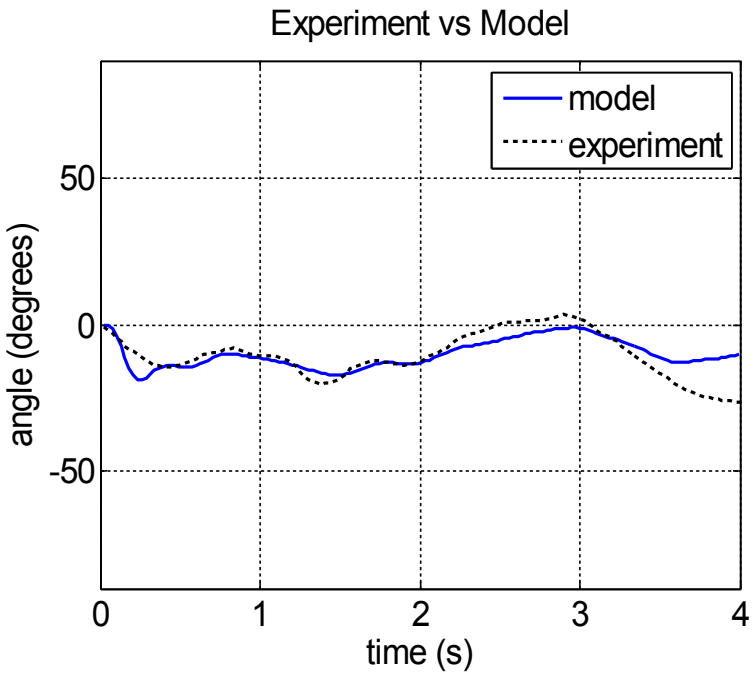

Figure 39: Flat wing theta angle response with a single support inflated with helium and augmented with vertical fin before turn

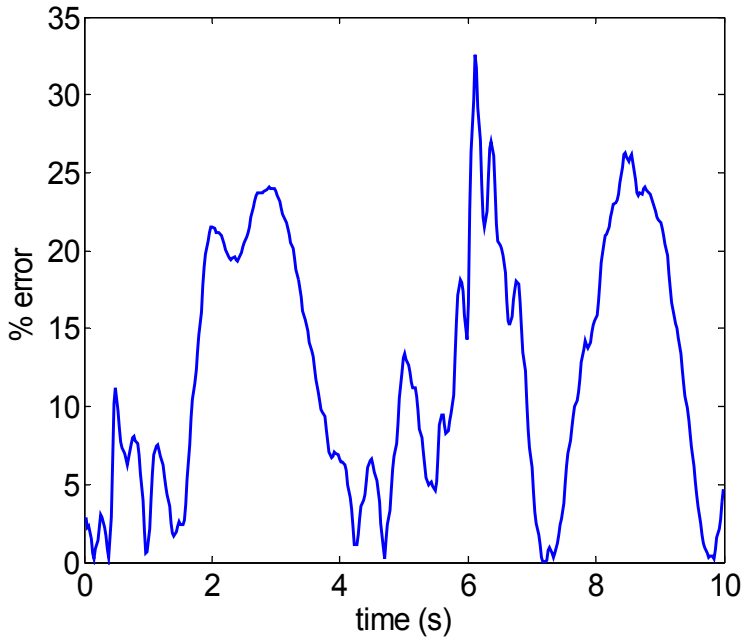

Figure 40: Error plot for Flat wing elevator input with a single support inflated with helium and augmented with vertical fin before turn

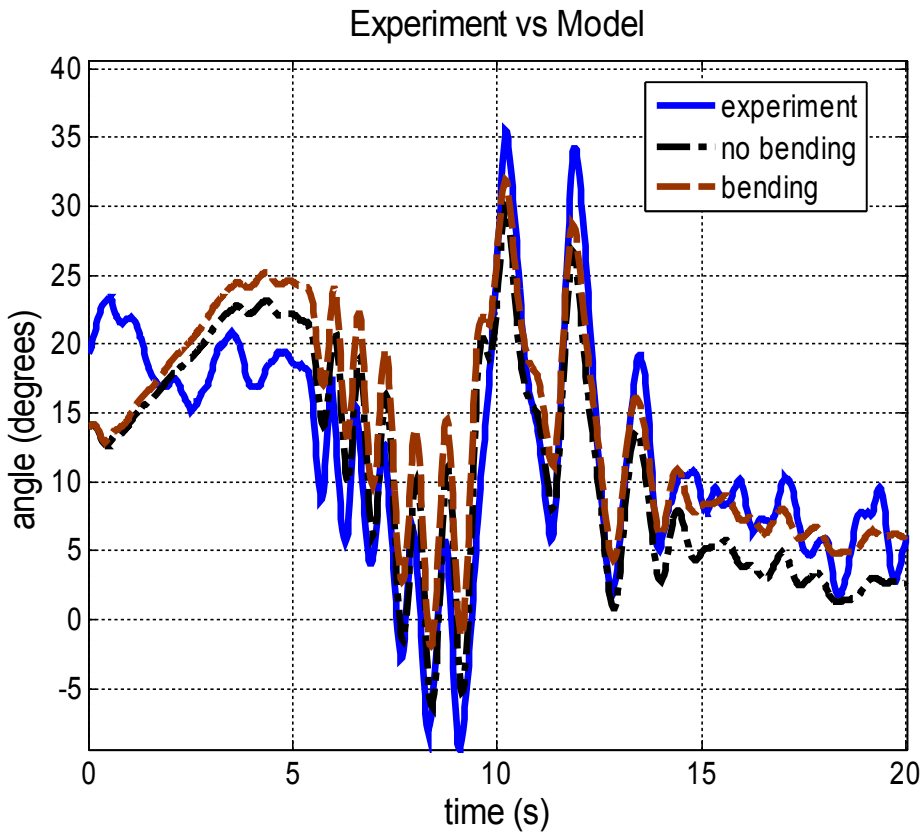

Figure 41: Bending mode dampens pitching motion with time

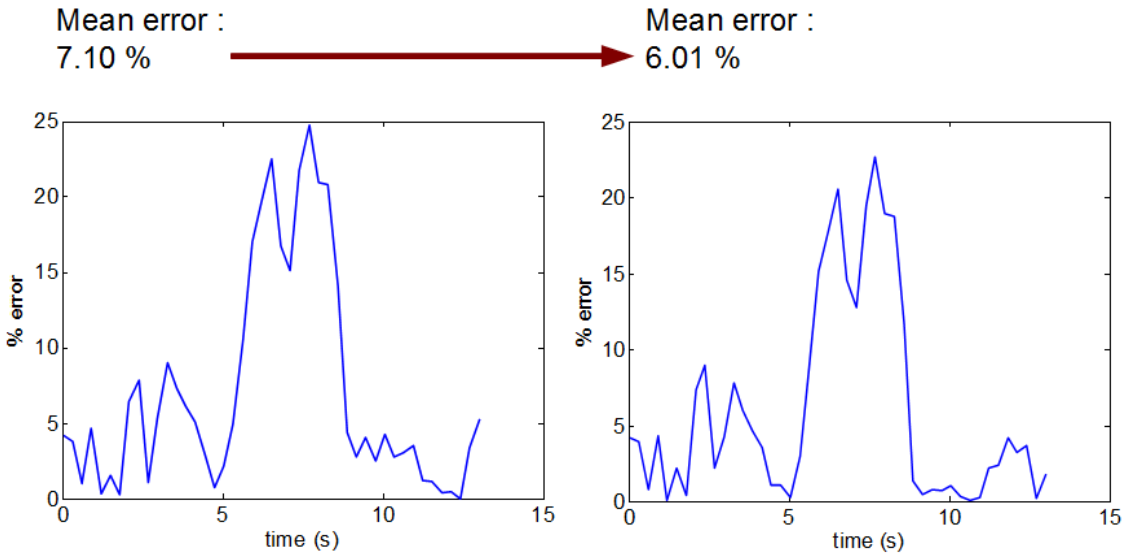

Figure **42:** Comparison of model error when doubling the value of $C_{M\eta}$

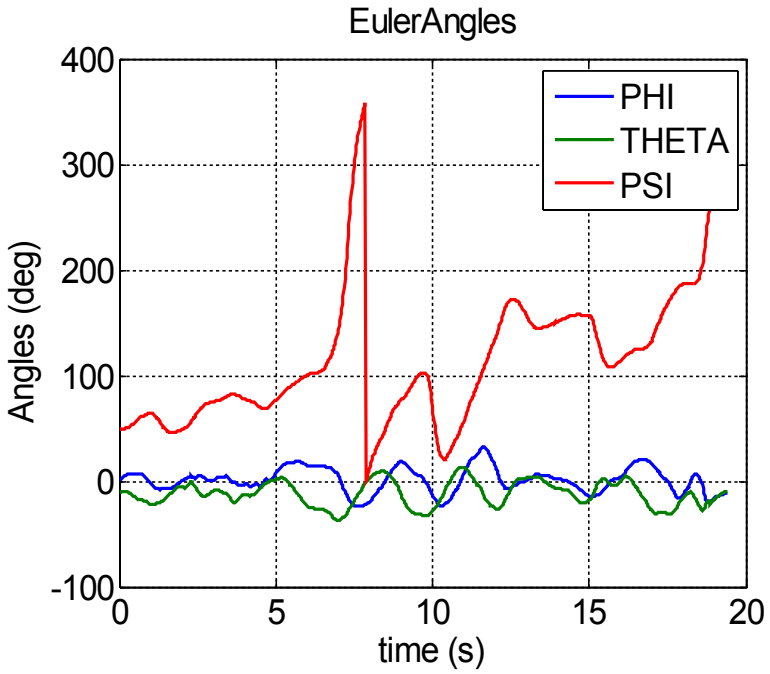

Figure **43:** Finned straight wing performing a turning maneuver

Several 3 degree of freedom models where implemented in Matlab for the purpose of matching flight test data collected. Integration was handled with a Runge-Kutta 4 scheme. Unless specified other wise, simulations where ran with a delta t of 0.0261 s for flight test data collected without GPS and at 0.025 s for flight test data collected with GPS. This difference is due to the limits GPS placed on telemetry update rate. Because the GPS limited data to 4 Hz, control inputs were later over-sampled by 10 times to conform the the higher update rates of the nonlinear simulation.

The following figures (figure 44-46) show the frequency response of the different platforms over the the range that is considered applicable to human piloted flight (0 - 12 rad/sec). Again, all frequency decomposition was done with the CIFER software package. The associated poles and damping ratios are given for each configuration.

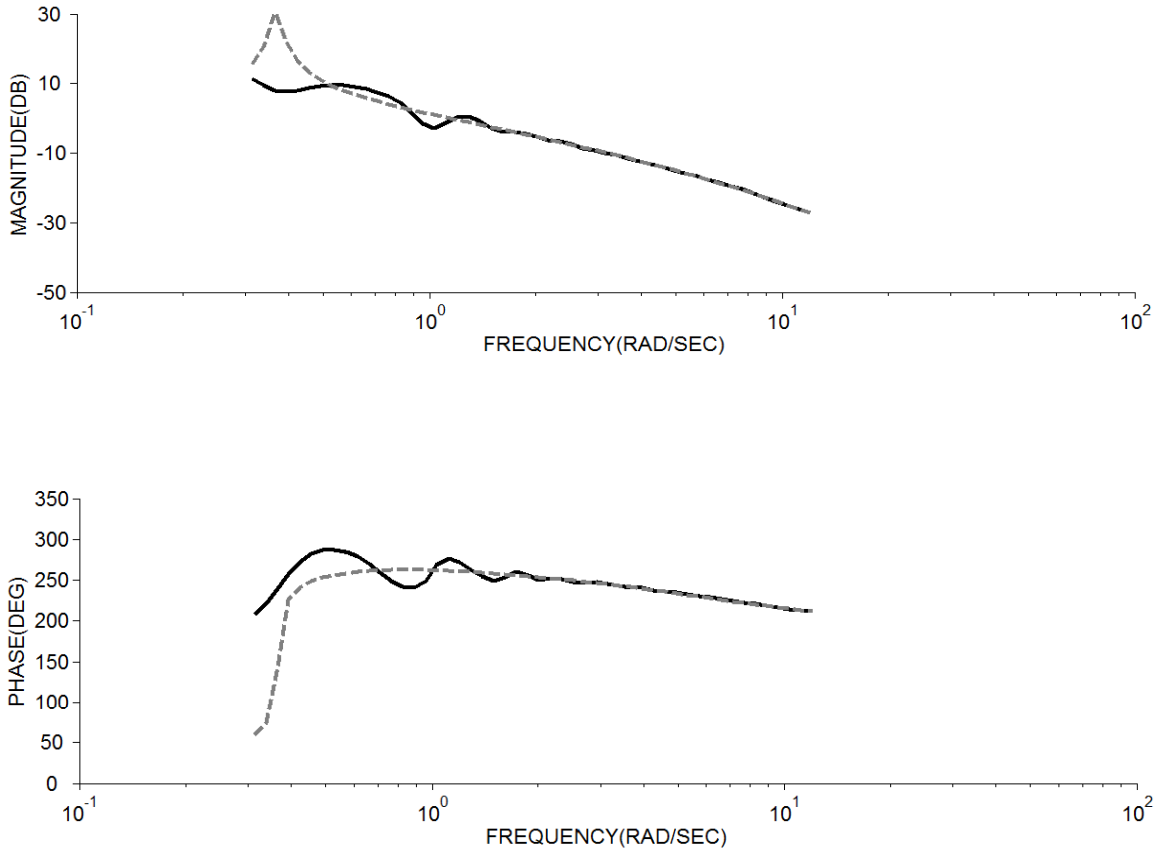

Figure 44: Magnitude and phase plot for simulation matching wing with a single support

flat wing

$$\frac{\theta}{\delta_e} = \frac{6.793\,s^2 + 119.749\,s + 422.686}{s^4 - 9.649\,s^3 + 49.493\,s^2 + 267.121\,s + 46.824} \tag{36}$$

with a time delay of 0.2984 seconds

Table 5.1: Modes for dihedral wing with carbon fiber supports

Natural Frequency (rad/s)	**Damping Ratio**
0.1816	1
2.9152	1
9.4040	-0.6777
9.4040	-0.6777

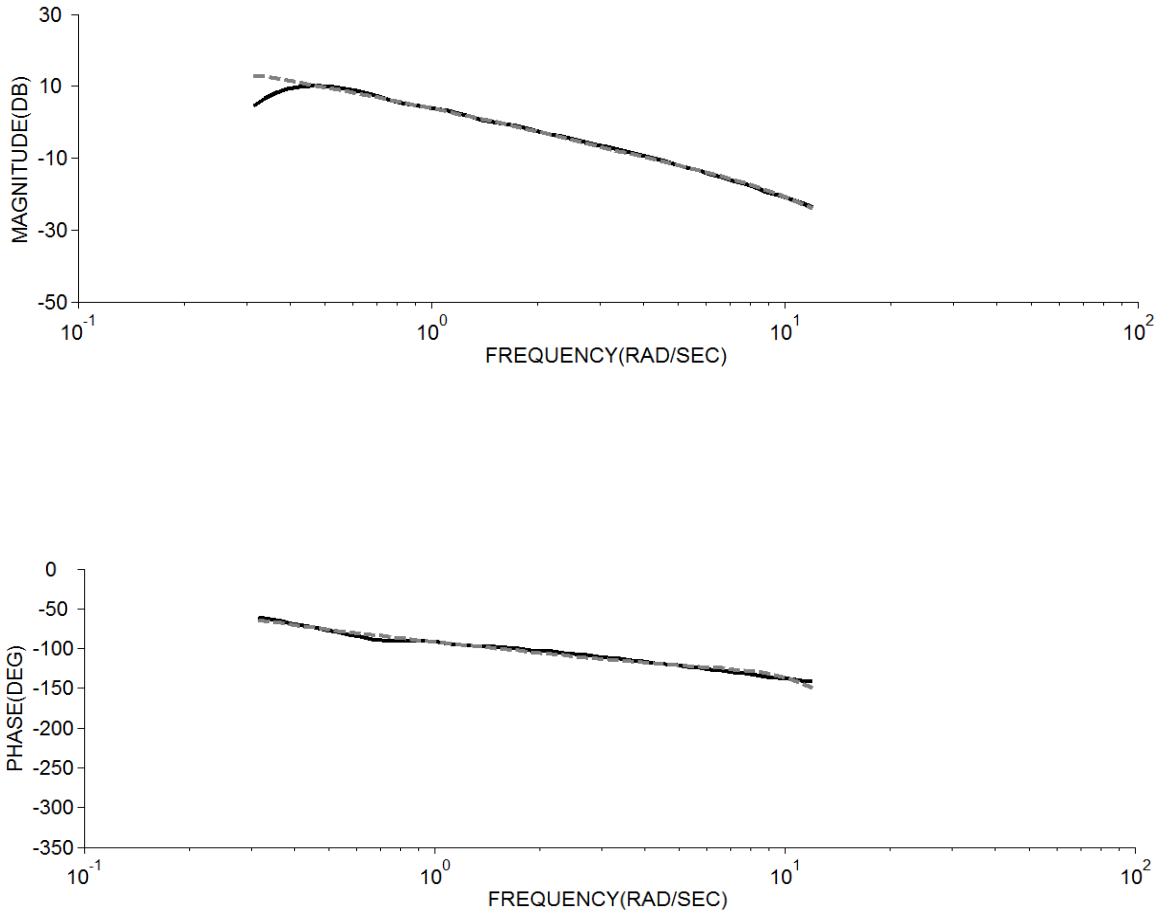

Figure 45: Magnitude and phase plot for simulation matching flat wing without supports

flat wing without support

$$\frac{\theta}{\delta_e} = \frac{7.041\,s^2 + 2.024\,s + 0.652}{s^4 + 6.508\,s^3 + 2.225\,s^2 + 0.832\,s + 0.298} \tag{37}$$

Table 5.2: Modes for flat wing without supports

Natural Frequency	**Damping Ratio**
0.36	1.00
0.3663	-0.0271
0.3663	-0.0271
6.1679	1

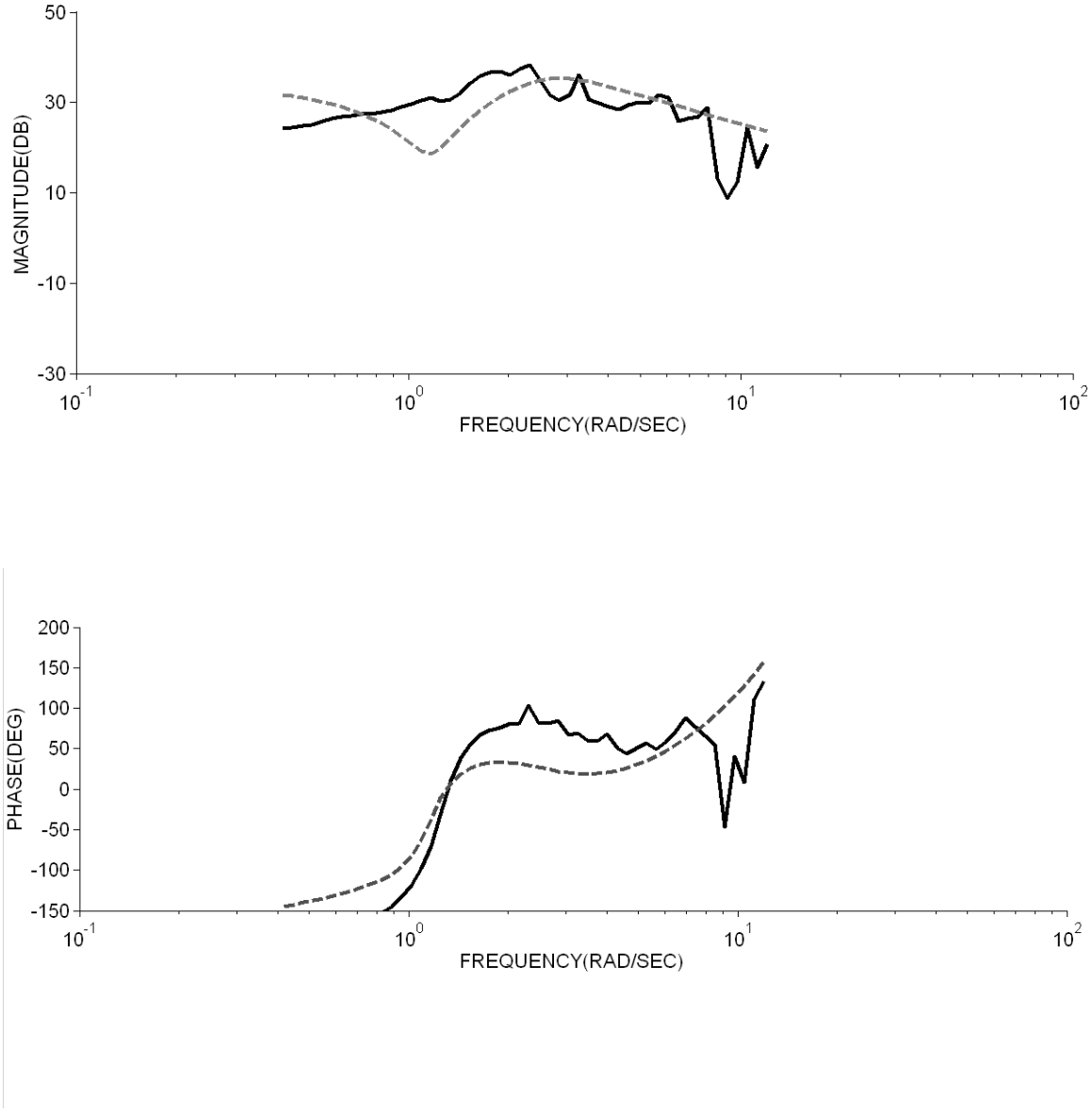

Figure 46: System ID of flight test data for single spar for qualitative comparison

5.2 NATASHA

Figures 47 to 50 show the finite difference modeling of the first bending mode of the bare inflatable wing in NATASHA. NATASHA does not have explicit methods for inflatable structures. As a result, the stiffness values approximated from the bench testing were placed into a script describing a cantilevered beam at 3 ft in length. This represented one half of the inflatable wing attached to the glider's fuselage. Each element of the wing

measured 0.3 ft long with a total of 10 segments and 11 nodes. Modeling the wing this way generated the lowest wing bending mode at approximately 23 radians per second. Figures 47 through 50 show the force and moment calculations along the wing with support carbon fiber structures at each node for all 3 orthogonal directions in the wing coordinate frame. This correlated well to the 3.5 Hz approximation made experimentally with the bench test. The scale on figures 47-50 have all been set to -1 to +1 on the y-axis to emphasize the the directions where non trivial values have been computed for forces and moments. In appendix C, the figures C.1 through C.9 do not have this scaling. Here, you can see some of the residual values for the moments calculated for the higher modal harmonics. All these values are at least several orders of magnitude smaller than the values of interest as expected and indicated by the scaling in the top left corner of each figure.

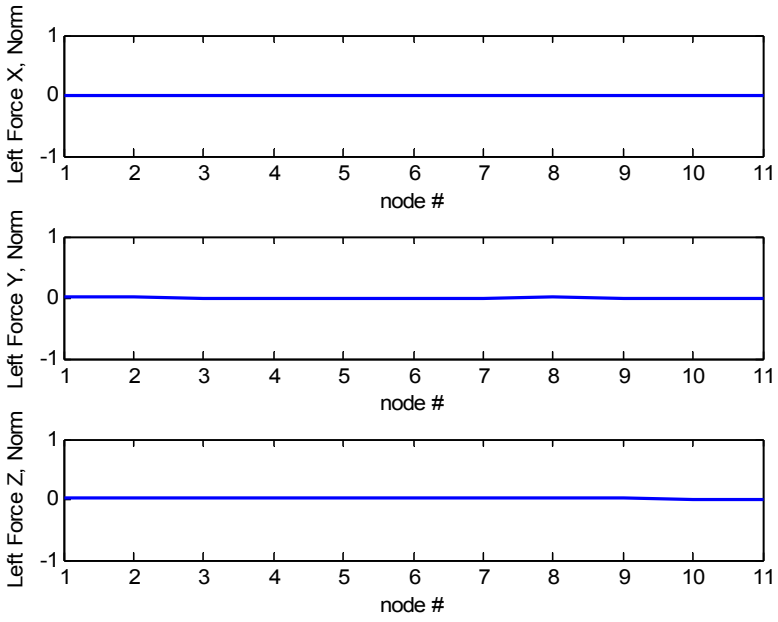

Figure 47: Forces from first bending mode in NATASHA

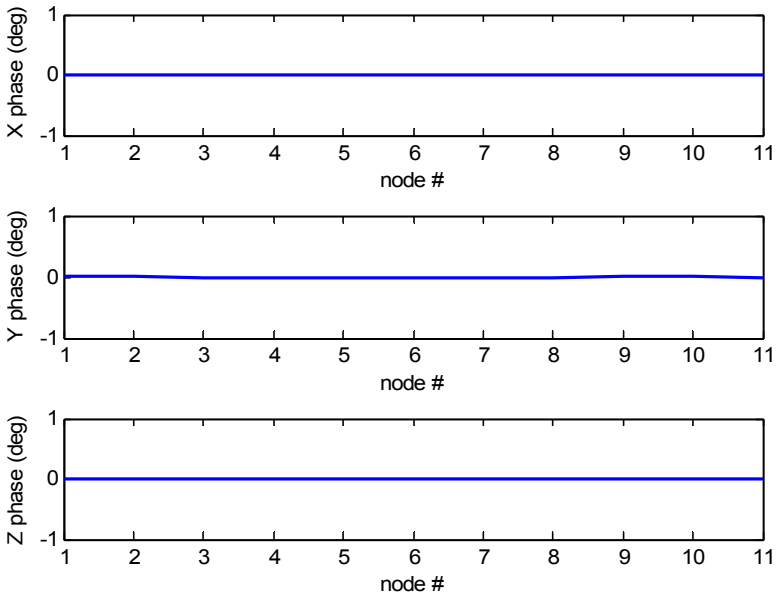

Figure 48: Phasing from forces of the first bending mode in NATASHA

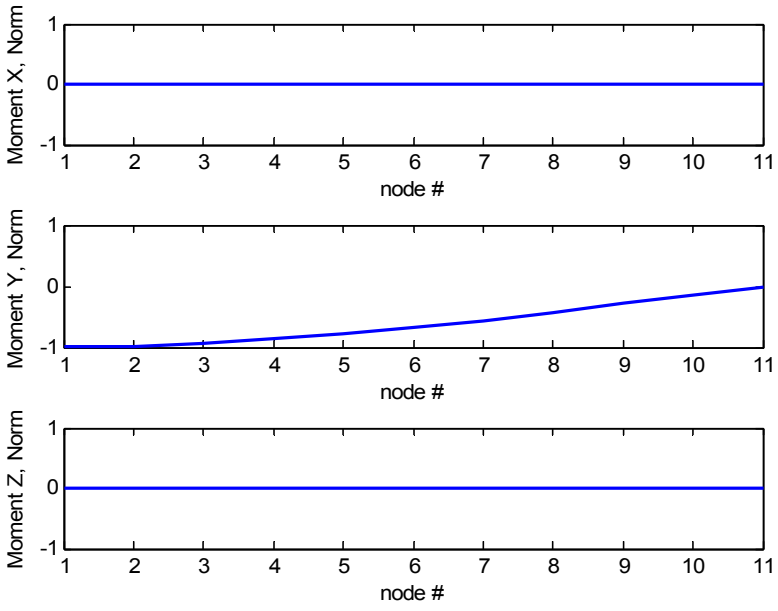

Figure 49: Moments from first bending mode in NATASHA

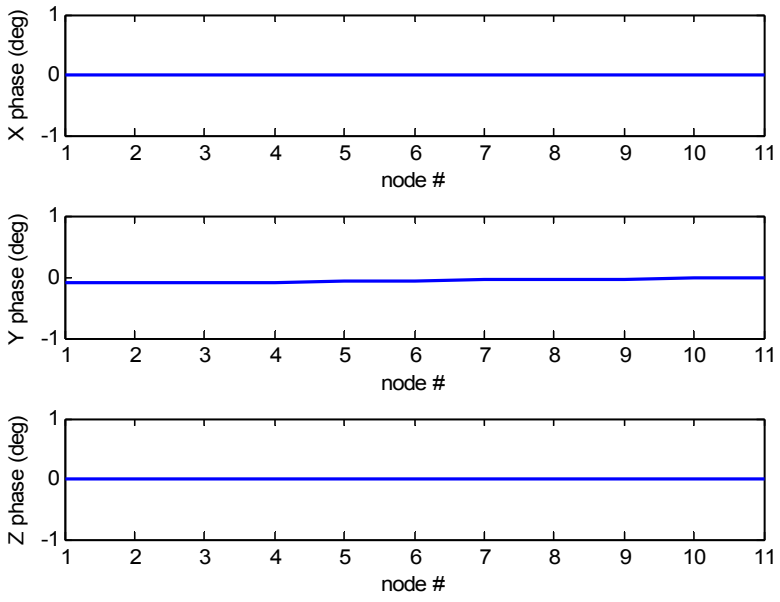

Figure 50: Phasing from moments of the first bending mode in NATASHA

The objective here was to make sure the first bending mode's frequency match that of the bending mode frequency of the experiment, where a cantilevered wing was mounted to a bench. A total of 51 bending modes where found with more than half being part of conjugate pairs in the eigenvalue analysis. The same wing was subjected to an unsteady flow analysis at standard atmospheric conditions, trimmed to 15 ft/s. The total number of bending modes saw a reduction to 30 modes, but the same fundamental frequency of 3.5 Hz remained. Again, the majority of these modes where part of complex conjugate pairs. Appendix A includes the code used to identify and isolate the bending modes. Appendix C includes the list of natural frequencies and damping ratios for the cantilevered wing in each case of no wind and trim conditions.

A sample of the recorded data on the experimental process of aquiring the first bending mode natural frequency is shown below, but for the wing without any support structures. In this case, the natural frequency of the wing is found to be significantly lower. In this case, it would be expected to see some coupling with the vehicles natural

frequency and those of the wing alone. As noted in the discussion above, when using CIFER, it was not uncommon to find frequencies of the vehicle in the range of 9 radians per second. The table below shows that the approximate natural frequency of the bare wing was about 1.6 Hz, or about 10 radians per second.

Table 5.4. Experimental data on cantilevered wing without supporting structures

Total time	**# of cycles**	**Hz**
2:30	4	1.7391
3:57	5	1.4006
2:39	4	1.6736
3:18	5	1.5723
1:86	3	1.6129
1:93	3	1.5544

CHAPTER 6

CONCLUSIONS

6. 1 SUMMARY

Both a simulation model and an experimental platform were designed and compared to gain quantitative and qualitative understanding on the unique characteristics of an inflatable wing aircraft with non-negligible flexibility in the main wing. The experimental platform proved to be a challenge that required a few design iterations before acceptable flight test data could be captured that represented the characteristics of each configuration. Though the test bed was not comparable to a militarily hardened fielded design in its durability, it was durable enough for a series of flights over several weeks. The flight regime it was able to attain was comparable to that which would be expected of a dismounted soldier's unmanned aerial system.

The unsteady characteristics of the aircraft's flight mechanics played a major roll in matching flight test data. Not only did the wing bending mode effect the accuracy of the results, but so did the rate of change in the vehicle's angle of attack. This was supported by the side to side comparison of the traditional wing being mounted on the glider platform versus the inflatable wing being mounted on the platform.

In the end, the quasi-steady model proved capable of making a respectible match to the flight test data for the inflatable wing platform. The quasi-steady model may thus be an adequate baseline for future platforms with similar flexibility in the wings and other aerodynamics surfaces.

6. 1 RECOMMENDED FUTURE WORK

In future work, it would be useful to expand this flight dynamics model to include more degrees of freedom in the wing's flexibility. Though the baseline analytical model used did not include any torsional bending modes, it was clear that for the case of the aircraft used in this work, that the addition of torsional aeroelastic modes would help to model more accurately. This mode was was observed visually and in the data from the flight test taken.

In future work, it is proposed that a more robust platform be designed for a similar price point for additional tests on elasticity on inflatable aircraft. It would also be worthwhile to design a feedback controller that takes into account this flexibility and assist in gust rejection to improve the stability and the flight envelope of similar vehicles. As noted in the literature review, some controllers have already been proposed to alleviated side effects of vehicles with large amounts of flexibility, especially in the wings. Personal interest in applications of nonlinear control theory, would likely lead to implementation of a feedback linearization scheme such as that proposed by Shearer and Cesnik [41]. It would be of interest to gauge the level of effectiveness of these controllers with different vehicle configurations similar to those explored in this thesis.

Lastly, the degraded aerodynamic performance of the inflatable wing configured as shown in this research has also lead to interest in some alternative wing designs, which might perhaps included baffles sealed in difference directions with respect to the wing chord. The addition of thin sheeting over the wing surface to improve the laminar flow characteristics on the wing surface could also be a promising subject of applied research in this area. Along these lines, a formalized error propagation (Appendix C) analysis would be beneficial in determining improvements to future related research projects.

APPENDIX A

CODE FOR DYNAMICS MODEL AND NATASHA ANALYSIS

```
% eigenvalue analysis script

close all;
clc;

disp('using parameters, eval_ab, evec_ab')

% Zahra Cantilever, using british system
% bending modes: 78 ~> 88

clearvars ModeValue ModeShape cntt nodeparams moments_dist
md_y_left...
    flag_bending

Mode = 101;
fprintf('mode to examine: %3.0f \n', Mode)

ModeValue  = eval_ab(Mode);
ModeShape = evec_ab(:,Mode);

[Wn, Zn] = damp(ModeValue);

fprintf('Natural Frequency: %3.2f rad/s \n', Wn)

fprintf('Damping Ratio: %3.4f \n', Zn)

cntt = (nm1/NN); % # modal paramters / # nodes
nodeparams = zeros(cntt,NN);

F_l = zeros(3,NN);
F_r = zeros(3,NN);
M_l = zeros(3,NN);
M_r = zeros(3,NN);
V_r = zeros(3,NN);
Omega_r = zeros(3,NN);
g_r = zeros(3,NN);
c_s = 1:1:NN;

rad2deg = 180/pi;
```

```
% ----------------------
% Detect bending modes
% ----------------------

% Isolate moments, or elements 7-12, NN times in eigenvector
column for
% all NN nodes

for i=1:length(eval_ab)
    for j = 1:NN
        moments_dist((1:6)+6*(j-1),i) = evec_ab((7+(21*(j-1))):
(12+(21*(j-1))),i);
    end
end

% Isolate the bending moment on the left side of the node
md_y_left = zeros(NN,length(eval_ab));
flag_bending = zeros(NN,length(eval_ab));

for i=1:length(eval_ab)
    for j = 1:NN
        md_y_left(j,i) = moments_dist(2+6*(j-1),i);
    end
end

for i=1:length(eval_ab)
    for j = 1:NN
        if abs(real(md_y_left(j,i))) > 0.1 &&
abs(real(md_y_left(j,i))) < 1.1
            flag_bending(j,i) = 1;
        end
    end
end

bending_modes = zeros(1,length(eval_ab));
bending_list = [];

for i=1:length(eval_ab)
    if sum(flag_bending(:,i)) >= 1
        bending_modes(i) = 1;
        bending_list = [bending_list; i];
    end
end

% ----------------------
```

```
for i = 1:NN
   nodeparams(:,i) = ModeShape((i*cntt)-(cntt-1):i*cntt);
   temp = nodeparams(:,i);
   F_l(:,i) = temp(1:3);
   F_r(:,i) = temp(4:6);
   M_l(:,i) = temp(7:9);
   M_r(:,i) = temp(10:12);
   V_r(:,i) = temp(13:15);
   Omega_r(:,i) = temp(16:18);
   g_r(:,i) = temp(19:21);
end

% ------------------------
% -- Plots for analysis %-
% ------------------------

h1 = figure('Name', 'F_L real');
subplot(3,1,1)
plot(real(F_l(1,:)), 'linewidth', 2)
xlabel('node #')
ylabel('Left Force X, Norm')
subplot(3,1,2)
plot(real(F_l(2,:)), 'linewidth', 2)
xlabel('node #')
ylabel('Left Force Y, Norm')
subplot(3,1,3)
plot(real(F_l(3,:)), 'linewidth', 2)
xlabel('node #')
ylabel('Left Force Z, Norm')

h2 = figure('Name', 'F_L imaginary' );
subplot(3,1,1)
plot(rad2deg*imag(F_l(1,:)), 'linewidth', 2)
xlabel('node #')
ylabel(' X phase (deg)')
subplot(3,1,2)
plot(rad2deg*imag(F_l(2,:)), 'linewidth', 2)
xlabel('node #')
ylabel(' Y phase (deg)')
subplot(3,1,3)
plot(rad2deg*imag(F_l(3,:)), 'linewidth', 2)
xlabel('node #')
ylabel('Z phase (deg)')
```

```
h3 = figure('Name', 'V real' );
subplot(3,1,1)
plot(real(V_r(1,:)), 'linewidth', 2)
xlabel('node #')
ylabel('Velocity X, Norm')
subplot(3,1,2)
plot(real(V_r(2,:)), 'linewidth', 2)
xlabel('node #')
ylabel('Velocity Y, Norm')
subplot(3,1,3)
plot(real(V_r(3,:)), 'linewidth', 2)
xlabel('node #')
ylabel('Velocity Z, Norm')

h4 = figure('Name', ' V imaginary' );
subplot(3,1,1)
plot(rad2deg*imag(V_r(1,:)), 'linewidth', 2)
xlabel('node #')
ylabel('X phase (deg)')
subplot(3,1,2)
plot(rad2deg*imag(V_r(2,:)), 'linewidth', 2)
xlabel('node #')
ylabel('Y phase (deg)')
subplot(3,1,3)
plot(rad2deg*imag(V_r(3,:)), 'linewidth', 2)
xlabel('node #')
ylabel('Z phase (deg)')

h5 = figure('Name', 'M_L real' );
subplot(3,1,1)
plot(real(M_l(1,:)), 'linewidth', 2)
xlabel('node #')
ylabel('Moment X, Norm')
subplot(3,1,2)
plot(real(M_l(2,:)), 'linewidth', 2)
xlabel('node #')
ylabel('Moment Y, Norm')
subplot(3,1,3)
plot(real(M_l(3,:)), 'linewidth', 2)
xlabel('node #')
ylabel('Moment Z, Norm')

h6 = figure('Name', ' M_L imaginary' );
subplot(3,1,1)
plot(rad2deg*imag(M_l(1,:)), 'linewidth', 2)
xlabel('node #')
```

```
ylabel('X phase (deg)')
subplot(3,1,2)
plot(rad2deg*imag(M_l(2,:)), 'linewidth', 2)
xlabel('node #')
ylabel('Y phase (deg)')
subplot(3,1,3)
plot(rad2deg*imag(M_l(3,:)), 'linewidth', 2)
xlabel('node #')
ylabel('Z phase (deg)')
```

Main Script for 3 DOF simulation with quasi-steady aero model

```
% Model to run Doam Electric glider with inflatable wing

% Based on B1 model
% B-1 Lancer flexible 3-Dof model
% Ref: 1988 Waszak & Schmidt
% Ref: coefficients per MGG

clc
clear all
close all

global deltaT Vo tempdata alpha_old

load('sample1.mat');
ThetaReal = (pi/180).*output(:,1);
ElevatorReal = output(:,2); % scaled -1 to +1
ElevatorReal = ElevatorReal*20; % convert to degrees

FoamEP_Params
t_total = 20; % total time, seconds, 1/0.01 rad/sec
timesteps = floor(t_total/deltaT);
Vo = 7; % 6
theta0 = 14*(pi/180);


x_trim = [ Vo*cos(theta0); Vo*sin(theta0); 0; theta0; 0; 0; 0; 0;
0; 0; 0];
x_old = x_trim;
x_dot = [ 0; 0; 0; 0; 0; 0; 0; 0; 0; 0; 0];
x_new = x_trim;
x_dot_hist = zeros(11,timesteps);
x_hist(:,1) = x_trim;
```

```
% u = GlideController(x_trim, 0);
u = [ElevatorReal(1); 0; 1];
% Initialize loads
% structural mode initial conditions

[Qloads2 out1] = GenForces(x_new, x_dot, u);
t_old = 0;
t = 0;

alpha_old = (180/pi).*atan2(x_trim(2), x_trim(1));

tempdata = zeros(7,timesteps);
elast = zeros(4,timesteps);

loads_hist = zeros(7,timesteps);
u_hist = zeros(3,timesteps);
time_hist = deltaT:deltaT:t_total;

% ui = ui_function(timesteps, time_hist);
ui = GlideController(x_trim, 0);
u_hist(:,1) = u;


hh = input('1 to stop, 2 to continue: ');

if hh ==1
    return
else
    disp('continue')
end

%  gh = 1;

% fig1 = figure('Name', 'animate');
% axis([-50 250 -600 50])
% [blat, blon] = boxxerDH(x_new(5),-x_new(7),x_new(4)*180/pi);
% pball=fill(blat,blon,'green','EraseMode','background');
tic

for jk = 2:timesteps

    % u = [5; 0; 1];

    u = [ElevatorReal(jk); 0; 1];
```

```
    % u = GlideController(x_new);

    [Qloads tempdata2] = GenForces(x_new, x_dot, u);
    loads_hist(:,jk) = Qloads';

    u_hist(:,jk) = u';

    [x_dot etas] = EqnOfMotAugTrun(x_new, Qloads, t);
    x_dot_hist(:,jk) = x_dot;
    elast(:,jk) = etas;

    % RK4 integration
    [x_dot1 etas1] = EqnOfMotAugTrun(x_new, Qloads, t);
    [x_dot2 etas2] = EqnOfMotAugTrun(x_new+0.5*x_dot1*deltaT,
Qloads, t+0.5*deltaT);
    [x_dot3 etas3] = EqnOfMotAugTrun(x_new+0.5*x_dot2*deltaT,
Qloads, t+0.5*deltaT);
    [x_dot4 etas4] = EqnOfMotAugTrun(x_new+x_dot3*deltaT, Qloads,
t+deltaT);

    k1 = deltaT*x_dot1;
    k2 = deltaT*x_dot2;
    k3 = deltaT*x_dot3;
    k4 = deltaT*x_dot4;

    s=(k1+2*k2+2*k3+k4)/6;
    state_derv = s/deltaT;

    x_new = x_old + s;
    x_hist(:,jk) = x_new;
    x_old = x_new;
    t_old = t;
    t = t_old + deltaT;

    temp(jk-1) = tempdata2;

end

% inertial postion

forward = x_hist(5,:);
down = x_hist(7,:);

fig1 = figure('Name','Speed');
plot(time_hist, x_hist(1,:), time_hist, x_hist(2,:), 'k--');
legend('U', 'W')
```

```
set(get(gca,'Children'),'linewidth',2)
set(gca,'FontSize',12,'Fontname','Times')
xlabel('time (s)')
ylabel('ft/s')
title('Body Velocity')

fig2 = figure('Name','Forward-Down');
plot(forward,-down, 'k--');
legend('Man 1', 'data')
set(get(gca,'Children'),'linewidth',2)
set(gca,'FontSize',12,'Fontname','Times')
xlabel('X (ft)')
ylabel('Z (ft)')
title('Position')
axis equal
grid on

rate_q = x_hist(3,:);

fig3 = figure('Name','pitch rate');
plot(time_hist, (180/pi)*rate_q, 'k')
legend('q ', 'data')
set(get(gca,'Children'),'linewidth',2)
set(gca,'FontSize',12,'Fontname','Times')
xlabel('time (s)')
ylabel('q (deg/s)')
title('q')
% ylim([-10 10])

fig4 = figure('Name','Euler Theta');
plot(time_hist, (180/pi).*x_hist(4,:), 'k--')
legend('Angle', 'data')
set(get(gca,'Children'),'linewidth',2)
set(gca,'FontSize',12,'Fontname','Times')
xlabel('time (s)')
ylabel('theta (deg)')
title('Theta')

fig5 = figure('Name','Control Input');
plot(time_hist, 1*u_hist(1,:), 'k:', time_hist, 1*u_hist(2,:),
'r', time_hist, 1*u_hist(3,:), 'b--')
legend('elevator', 'rudder', 'throttle')
set(get(gca,'Children'),'linewidth',2)
set(gca,'FontSize',12,'Fontname','Times')
xlabel('time (s)')
ylabel('delta')
```

```
title('Input Vector U')
grid on

fig6 = figure('Name', 'Comparison');
plot(time_hist, (180/pi)*ThetaReal(1:jk), time_hist,
(180/pi).*x_hist(4,:), 'k:')
legend('model', 'experiment')
set(get(gca,'Children'),'linewidth',2)
set(gca,'FontSize',12,'Fontname','Times')
xlabel('time (s)')
ylabel('angle (degrees)')
title('Experiment vs Model')
grid on
```

Loads Calculation (GenForces.m)

```
function [out1 param] = GenForces(x, x_dot, u_i)


global c_bar S rho Vo Keta...
    C_X_0 C_X_alpha C_X_alphadot C_X_q C_X_delta_e C_X_eta1
C_X_eta2...
    C_X_eta3 C_X_eta4 C_X_etadot1 C_X_etadot2 C_X_etadot3
C_X_etadot4...
    C_Z_0 C_Z_alpha C_Z_alphadot C_Z_q C_Z_delta_e C_Z_eta1
C_Z_eta2...
    C_Z_eta3 C_Z_eta4 C_Z_etadot1 C_Z_etadot2 C_Z_etadot3
C_Z_etadot4...
    C_M_0 C_M_alpha C_M_alphadot C_M_q C_M_delta_e C_M_eta1
C_M_eta2...
    C_M_eta3 C_M_eta4 C_M_etadot1 C_M_etadot2 C_M_etadot3
C_M_etadot4...
    C_eta_0 C_eta_alpha C_eta_alphadot C_eta_q C_eta_delta_e
C_eta_eta1 C_eta_eta2...
    C_eta_eta3 C_eta_eta4 C_eta_etadot1 C_eta_etadot2
C_eta_etadot3 C_eta_etadot4...
    C_Z_w C_X_u C_Z_u alpha_old deltaT


delta_e = u_i(1);
delta_thr = u_i(3);

Pro = GenPro(delta_thr);
T_x = Pro(1);
T_z = Pro(3);
```

```
T_m = Pro(5);

u = x(1);
w = x(2);
q = x(3);
theta = x(4);
eta1 = x(8);
eta2 = x(9);
eta3 = x(10);
eta4 = x(11);
alpha = (180/pi).*atan2(w,u);
alphadot = (alpha-alpha_old)/deltaT;
etadot1 = x_dot(8);
etadot2 = x_dot(9);
etadot3 = x_dot(10);
etadot4 = x_dot(11);



Q_x = (rho*Vo^2*S/2)*(C_X_0 + C_X_u*u + C_X_alpha*alpha + ...
    C_X_delta_e*delta_e + C_X_eta1*eta1) + (rho*Vo*S*c_bar/4)*...
    (C_X_alphadot*alphadot + C_X_q*q + C_X_etadot1*etadot1) +
T_x;

Q_z = (rho*Vo^2*S/2)*(C_Z_0 + C_Z_u*u + C_Z_w*w + C_Z_alpha*alpha
+ ...
    C_Z_delta_e*delta_e + C_Z_eta1*eta1) + (rho*Vo*S*c_bar/4)*...
    (C_Z_alphadot*alphadot + C_Z_q*q + C_Z_etadot1*etadot1) +
T_z;

Q_theB = (rho*Vo^2*S*c_bar/2)*(C_M_0 + C_M_alpha*alpha + ...
    C_M_delta_e*delta_e + C_M_eta1*eta1) +
(rho*Vo*S*c_bar*c_bar/4)*...
    (C_M_alphadot*alphadot + C_M_q*q + C_M_etadot1*etadot1) +
T_m;

Q_eta1 = Keta*(rho*Vo^2*S*c_bar/2)*(C_eta_0(1) +
C_eta_alpha(1)*alpha + ...
    C_eta_delta_e(1)*delta_e + C_eta_eta1(1)*eta1)+
(rho*Vo*S*c_bar*c_bar/4)*...
    (C_eta_alphadot(1)*alphadot + C_eta_q(1)*q +
C_eta_etadot1(1)*etadot1);


%%%
```

```
Q_eta2 = Keta*(rho*Vo^2*S*c_bar/2)*(C_eta_0(2) +
C_eta_alpha(2)*alpha + ...
    C_eta_delta_e(2)*delta_e + C_eta_eta1(2)*eta1 +
C_eta_eta2(2)*eta2 + ...
    C_eta_eta3(2)*eta3 + C_eta_eta4(2)*eta4) +
(rho*Vo*S*c_bar*c_bar/4)*...
    (C_eta_alphadot(2)*alphadot + C_eta_q(2)*q +
C_eta_etadot1(2)*etadot1 +...
    C_eta_etadot2(2)*etadot2 + C_eta_etadot3(2)*etadot3 +
C_eta_etadot4(2)*etadot4);

Q_eta3 = Keta*(rho*Vo^2*S*c_bar/2)*(C_eta_0(3) +
C_eta_alpha(3)*alpha + ...
    C_eta_delta_e(3)*delta_e + C_eta_eta1(3)*eta1 +
C_eta_eta2(3)*eta2 + ...
    C_eta_eta3(3)*eta3 + C_eta_eta4(3)*eta4) +
(rho*Vo*S*c_bar*c_bar/4)*...
    (C_eta_alphadot(3)*alphadot + C_eta_q(3)*q +
C_eta_etadot1(3)*etadot1 +...
    C_eta_etadot2(3)*etadot2 + C_eta_etadot3(3)*etadot3 +
C_eta_etadot4(3)*etadot4);

Q_eta4 = Keta*(rho*Vo^2*S*c_bar/2)*(C_eta_0(4) +
C_eta_alpha(4)*alpha + ...
    C_eta_delta_e(4)*delta_e + C_eta_eta1(4)*eta1 +
C_eta_eta2(4)*eta2 + ...
    C_eta_eta3(4)*eta3 + C_eta_eta4(4)*eta4) +
(rho*Vo*S*c_bar*c_bar/4)*...
    (C_eta_alphadot(4)*alphadot + C_eta_q(4)*q +
C_eta_etadot1(4)*etadot1 +...
    C_eta_etadot2(4)*etadot2 + C_eta_etadot3(4)*etadot3 +
C_eta_etadot4(4)*etadot4);

param = [alphadot];

alpha_old = alpha;
out1 = [Q_x Q_z Q_theB Q_eta1 0 0 0];
```

Coefficient Calculation code

```
% Coefficients based of Waszak, Schmidt aerodynamic model, see
doc.
% Example calculation for B-1 Lancer model in Waszak, Schmidt,
1988
syms phi_x

close all
clear all
clc

b = 70; % ft
c = 15.3; % ft
S = 1947; % ft^2
e = 5-0.13; % ft, per figure 2 of Waszak, Schmidt
delta_x = -5; % -5
i_s = -1*(pi/180); % angle of incidence
e_ow = 0.95; % Oswalt efficiency factor, too low, and C_X's
change sign
ARw = (b*b/S);

U = 450; % trim speed, ft/s

Cl_o = 0;
Cl_alpha = 2*pi; % lift curve slope
Cl_delta = 0.185; % ???
e_delta = 0; % ?? N/A for wing
Cmac = -0.46;

alpha1 = 0.3; % rad per Wasak and Schmidt* (just alpha1, alpha in
deg o/w)

% PLUS EFFECTS DUE TO DIHEDRAL? take the cosine of the lift
component

% DRAG COMPONENT?

C_L_o = b/S*(Cl_o + Cl_alpha*i_s)*c;
C_L_alpha = (b/S)*Cl_alpha*c;
C_L_p = C_L_alpha*b^2*c/(8*S*U);
%C_L_q = (b/S)*(Cl_alpha*c*(delta_x+e)/U); % * 20000
C_L_q = (b/S)*(Cl_alpha*c*(500)/U);
```

```
C_L_delta = b/S*(Cl_delta*c);
% flexible dof coefficients
poly1 = -4.13e-4*(b/2)^3 + 0.0137*(b/2)^2 - 0.029*(b/2) - 0.0262;
poly2 = -4.13e-4*(-b/2)^3 + 0.0137*(-b/2)^2 - 0.029*(-b/2) -
0.0262;
C_L_eta_1 = 1/S*Cl_alpha*c*(poly1-poly2);
polyint1 = -4.13e-4/4*(b/2)^4 + 0.0137/3*(b/2)^3 -
(0.029/2)*(b/2)^2 +0.0262*(b/2);
polyint2 = -4.13e-4/4*(-b/2)^4 + 0.0137/3*(-b/2)^3 -(0.029/2)*(-
b/2)^2 +0.0262*(-b/2);
C_L_etadot_1 = 1/S*Cl_alpha/U*(polyint1-polyint2);
%-----------------------------------------------------------------
----------
C_M_o = b*c/(S)*(Cmac +(Cl_o + Cl_alpha*i_s)*((delta_x+e)/c));
C_M_alpha = b/S*(Cl_alpha*(delta_x + e));
% C_M_alpha = b/S*(Cl_alpha*(-0.13));
C_M_p = 0;
C_M_q = -b/(S)*Cl_alpha*(delta_x+e)^2/U; % incorrect in WS, right
in MGG
C_M_delta = (b)/S*(delta_x - e_delta);
% flexible dof coefficients
C_M_eta_1 = (1/S)*Cl_alpha*((delta_x+e))*(poly1-poly2);
C_M_etadot_1 = (1/(S))*Cl_alpha*((delta_x+e)/U)*(polyint1 -
polyint2);
%----------------------CD eqn's ref MGG Thesis
1982-------------------------
K = 1/(pi*ARw*e_ow);
CL1 = C_L_o + C_L_alpha*alpha1;
C_D_o = 2*K*CL1*C_L_o;
C_D_alpha = 2*K*CL1*C_L_alpha;
C_D_p = 2*K*CL1*C_L_p;
C_D_q = 2*K*CL1*C_L_q;
C_D_delta = 2*K*CL1*C_L_delta;
C_D_eta_1 = 2*K*CL1*C_L_eta_1;
C_D_etadot_1 = 2*K*CL1*C_L_etadot_1;

%-----------------------------------------------------------------
----------
C_X_o = (C_L_o*sin(alpha1) - C_D_o*cos(alpha1));
C_X_alpha = (pi/180)*(C_L_alpha*sin(alpha1) -
C_D_alpha*cos(alpha1));
C_X_q = (C_L_q*sin(alpha1) - C_D_q*cos(alpha1));
C_X_delta = (C_L_delta*sin(alpha1) - C_D_delta*cos(alpha1));
C_X_eta_1 = (C_L_eta_1*sin(alpha1) - C_D_eta_1*cos(alpha1));
C_X_etadot_1 = (C_L_etadot_1*sin(alpha1) -
C_D_etadot_1*cos(alpha1));
```

```
%-----------------------------------------------------------------
----------
C_Z_o = (-C_L_o*cos(alpha1) - C_D_o*sin(alpha1));
C_Z_alpha = (pi/180)*(-C_L_alpha*cos(alpha1) -
C_D_alpha*sin(alpha1));
C_Z_q = (-C_L_q*cos(alpha1) - C_D_q*sin(alpha1))*1;
C_Z_delta = (-C_L_delta*cos(alpha1) - C_D_delta*sin(alpha1));
C_eta_1 = (-C_L_eta_1*cos(alpha1) - C_D_eta_1*sin(alpha1));
C_etadot_1 = (-C_L_etadot_1*cos(alpha1) -
C_D_etadot_1*sin(alpha1));
%-----------------------------------------------------------------
----------
```

Equations of Motion (EqnOfMotAugTrun.m)

```
function [ xdot etas] = EqnOfMotAugTrun( x, Qvec, t )

% The augmented equations of motion
% Detailed explanation goes here

global Mass g Ixx Iyy Izz Ixy Iyz Ixz omega_1 omega_2 omega_3...
    omega_4 M_1 M_2 M_3 M_4 Mass_x Mass_z

 xdot = zeros(11,1);
 u = x(1);
 v = 0;
 w = x(2);
 p = 0;
 q = x(3);
 r = 0;
 phi = 0;
 theta = x(4);
 psi = 0;

 sphi = sin(phi);
 cphi = cos(phi);
 sthe = sin(theta);
 cthe = cos(theta);
 spsi = sin(psi);
 cpsi = cos(psi);


 Q_x = Qvec(1);
 Q_z = Qvec(2);
 Q_theB = Qvec(3);
```

```
 Q_eta1 = Qvec(4);
 Q_eta2 = Qvec(5);
 Q_eta3 = Qvec(6);
 Q_eta4 = Qvec(7);

 % Body axis velocities

 xdot(1) = Q_x/Mass_x - q*w - g*sthe;
 xdot(2) = Q_z/Mass_z + q*u + g*cthe;

 % Body axis rates

 xdot(3) = Q_theB/Iyy; %- ((Ixy*Ixz + Ixx*Iyz)*( Ixy*(p^2 - q^2)
+ r*(Iyz*p - Ixz*q) + p*q*(Ixx - Iyy)))/(Izz*Ixy^2 ...
%      + 2*Ixy*Ixz*Iyz + Iyy*Ixz^2 + Ixx*Iyz^2 - Ixx*Iyy*Izz) -
((Ixz*Iyz + Ixy*Izz)*( Iyz*(q^2 - r^2) ...
%      + p*(Ixz*q - Ixy*r) + q*r*(Iyy - Izz)))/(Izz*Ixy^2 +
2*Ixy*Ixz*Iyz + Iyy*Ixz^2 + Ixx*Iyz^2 - Ixx*Iyy*Izz) ...
%      - ((Ixz^2 - Ixx*Izz)*(Ixz*(p^2 - r^2) - Q_theB + q*(Iyz*p
- Ixy*r) + p*r*(Ixx - Izz)))/(Izz*Ixy^2 + 2*Ixy*Ixz*Iyz ...
%      + Iyy*Ixz^2 + Ixx*Iyz^2 - Ixx*Iyy*Izz);

 % Attitudes

 xdot(4)= q*cphi-r*sphi;

 % Positions

 xdot(5)= u*cthe*cpsi+v*(sphi*sthe*cpsi-cphi*spsi)
+w*(cphi*sthe*cpsi+sphi*spsi);
 xdot(6)= u*cthe*spsi+v*(sphi*sthe*spsi+cphi*cpsi)
+w*(cphi*sthe*spsi-sphi*cpsi);
 xdot(7)= -u*sthe + w*1*cthe;

 % Elastic mode
 xdot(8) = Q_eta1/(omega_1*omega_1*M_1)*sin(omega_1*t);
 xdot(9) = 0; % Q_eta2/(omega_2*omega_2*M_2)*sin(omega_2*t);
 xdot(10) = 0; % Q_eta3/(omega_3*omega_3*M_3)*sin(omega_3*t);
 xdot(11) = 0; % Q_eta4/(omega_4*omega_4*M_4)*sin(omega_4*t);

 etas(1) = Q_eta1/(omega_1*omega_1*M_1)*sin(omega_1*t);
 etas(2) = Q_eta2/(omega_2*omega_2*M_2)*sin(omega_2*t);
 etas(3) = Q_eta3/(omega_3*omega_3*M_3)*sin(omega_3*t);
 etas(4) = Q_eta4/(omega_4*omega_4*M_4)*sin(omega_4*t);

end
```

APPENDIX B

PLATFORM SCHEMATIC

Table B.1: Additional Platform description

Name	**Value**
Material	EPP foam
Weight	2.5 lbs
Power	900 mAh LiPo
Propeller	7 inch

Table B.2. Vehicle approximated inertia tensor w/ rigid wing in lbs*ft

Ixx = 3.54	Ixy = 0.00	Ixz = 0.03
Iyx = 0.00	Iyy = 1.61	Iyz = 0.00
Izx = 0.03	Izy = 0.00	Izz = 2.08

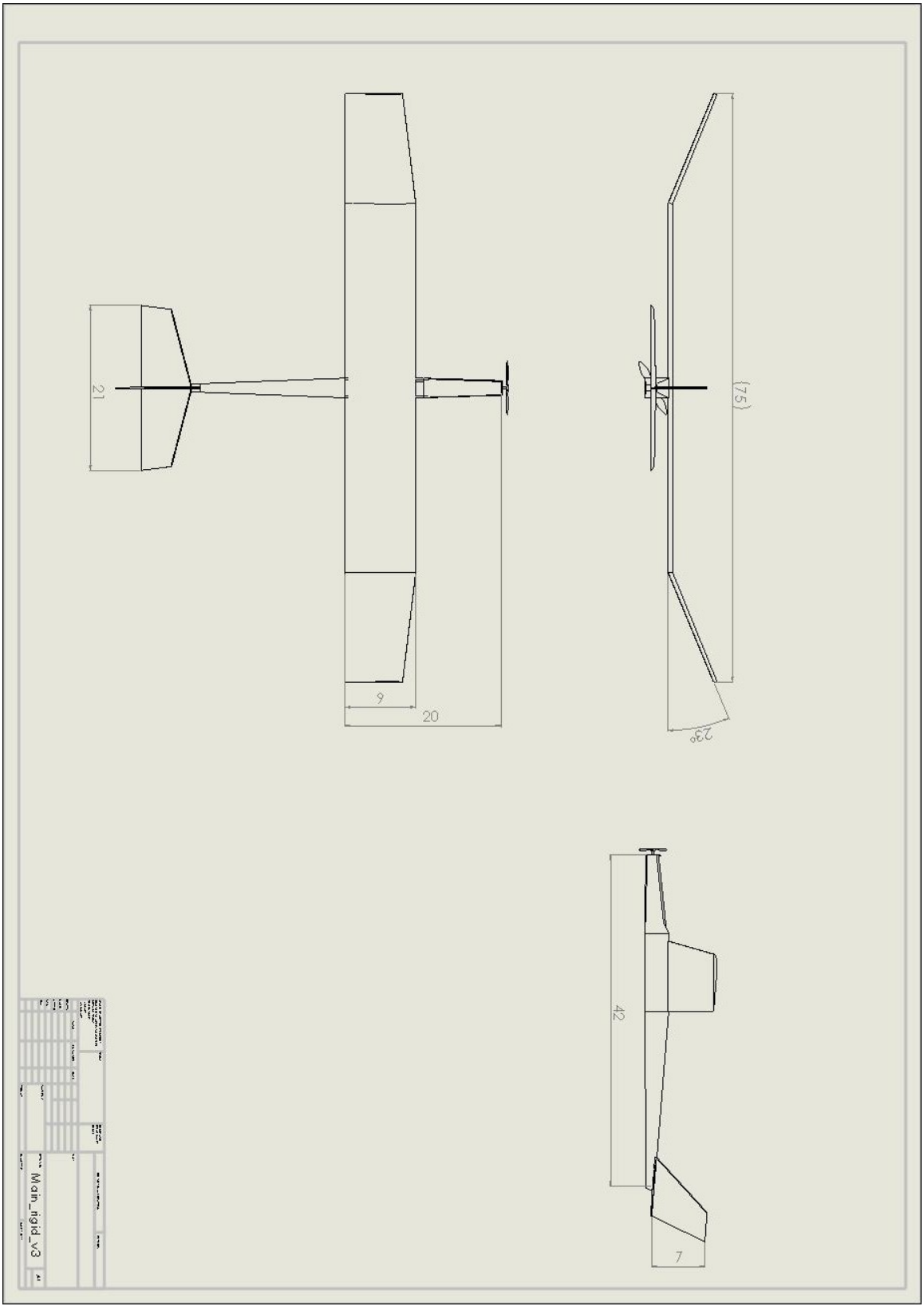

Figure B.1 Glider drawing with dimensions

APPENDIX C

Table C.1: First 10 bending modes in NATASHA for cantilevered wing in vacuum with carbon rod supports (mode number is from set which includes torsional modes and axial modes as well as in-plane bending)

Mode # (overall)	Frequency (rad/s)
101	23.68
93	72.45
85	127.62
81	189.20
75	264.27
71	362.44
67	505.44
61	747.88
53	1290.57
37	3937.01

Table C.2: First 10 bending modes in NATASHA for cantilevered wing at trim

Mode # (overall)	Frequency (rad/s)
75	23.68
69	72.45
65	127.62
59	189.20
55	264.27
47	362.44
43	505.44
39	747.88
31	1290.57
19	3937.01

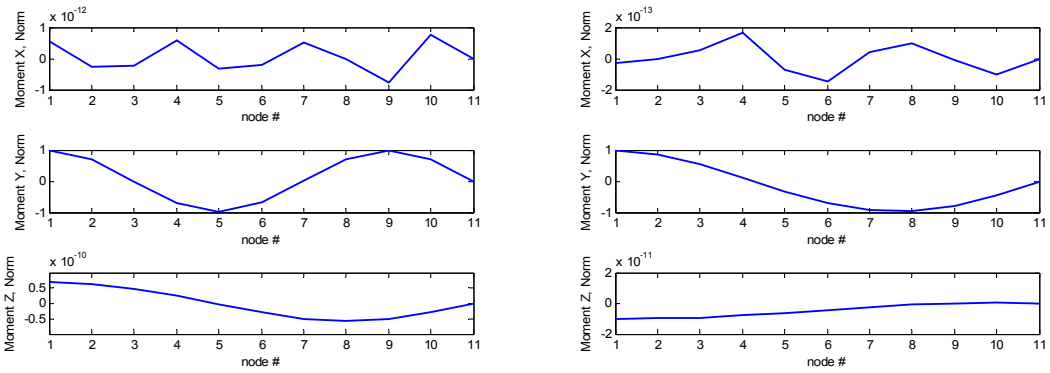

Figures C1, C2: 2nd and 3rd bending mode of cantilevered wing

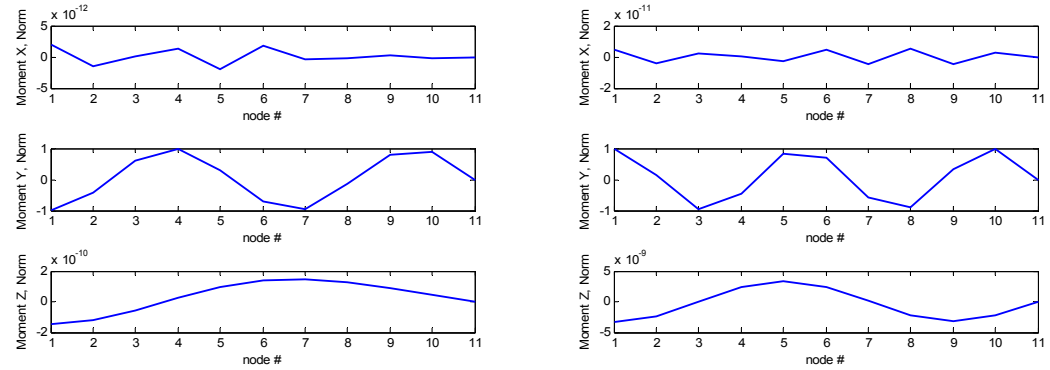

Figures C3, C4: 4th and 5th bending mode of cantilevered wing

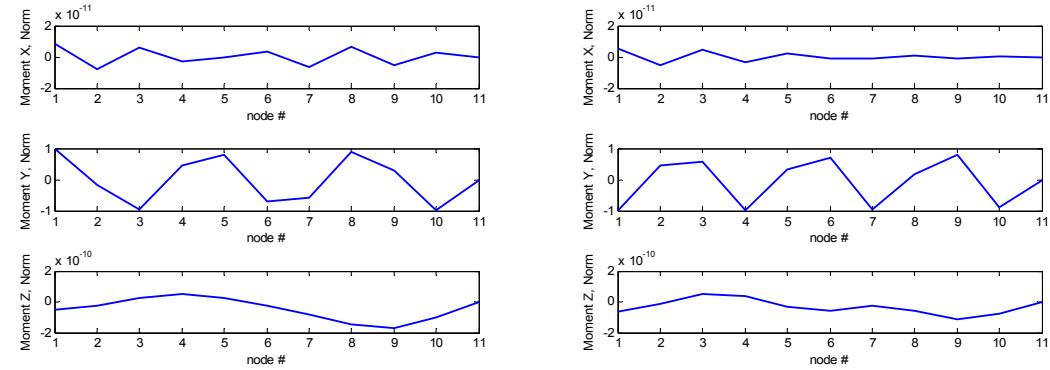

Figures C5, C6: 6th and 7th bending mode of cantilevered wing

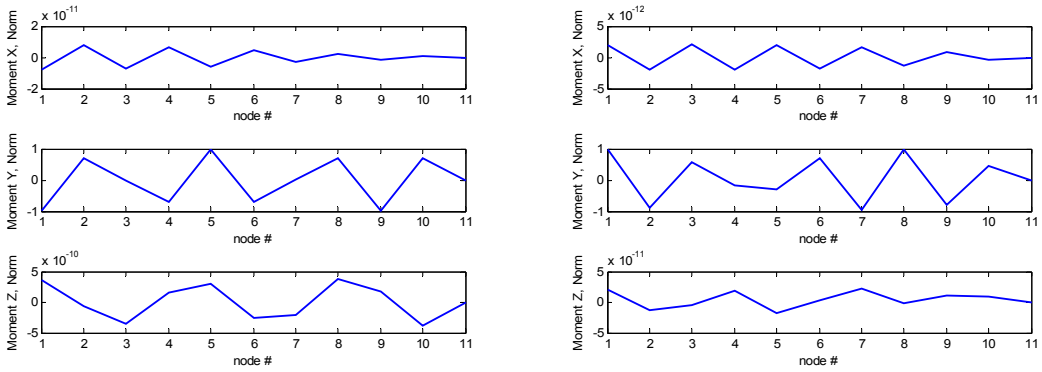

Figures C7, C8: 8th and 9th bending mode of cantilevered wing

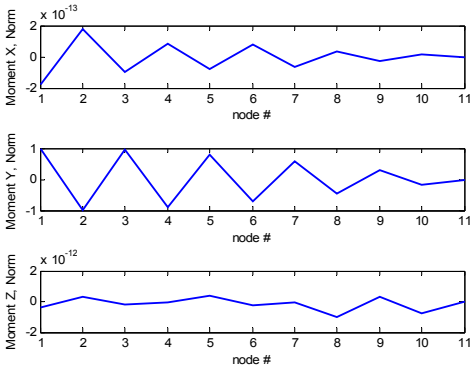

Figures C9: 10th bending mode of cantilevered wing

Table C.3 Coefficient tuning example

$\dot{\alpha}, C_{M\dot{\alpha}}$	- Rigid wing: 9.3, Inflatable wing: 11.73
$\eta, C_{M\eta}$	- Rigid wing: 0, Inflatable wing with supports: -0.03, Inflatable wing without supports: -3.21
$\dot{\eta}, C_{M\dot{\eta}}$	- Rigid wing: 0, Inflatable wing with supports: -0.159, Inflatable wing without supports: -0.349

Table C.4 Error Propagation Sources
(Useful for more advanced error analysis in the future)

Sources of error (process based and system based)
Wind (gusting up to 10 mph)
Temperature
Sensor noise (small MEMS device)
Sensor resolution
Data capturing frequency
Drift and bias

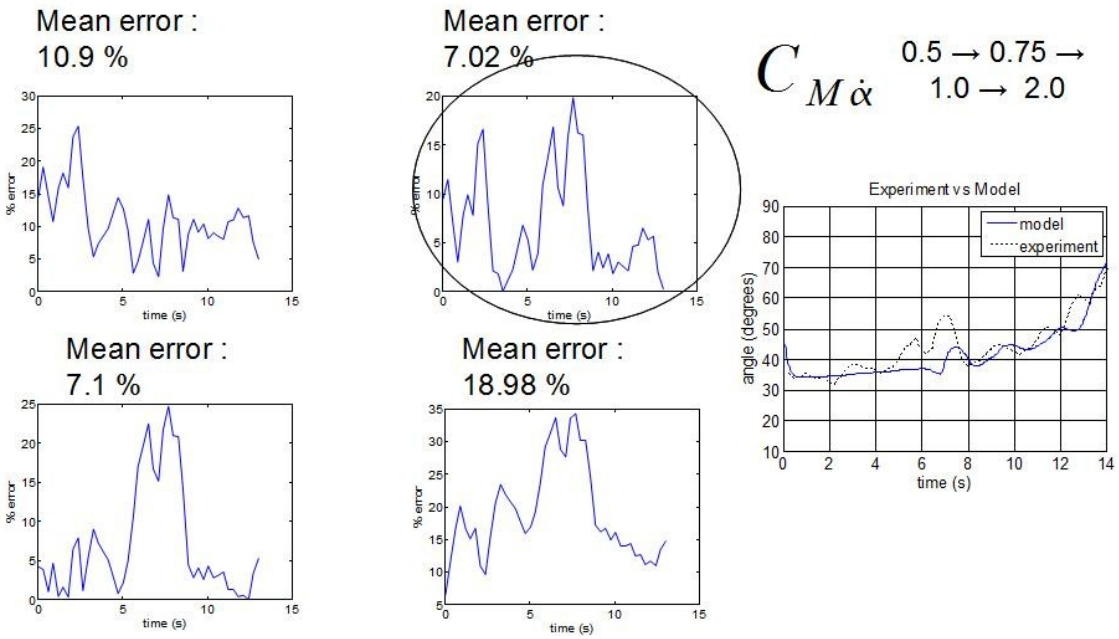

Figure C.10. Example of coefficient tuning process

REFERENCES

[1] EDGE, H, ET. AL., "Lighter-Than-Air and Pressurized Structures Technology for Unmanned Aerial Vehicles (UAVs)", Army Research Lab Technical Report, 2010.

[2] WINCHESTER, J. The World's Worst Aircraft: from Pioneering Failures to Multimillion Dollar Disasters, London: Amber Books Ltd., 2005.

[3] FUKUSHIMA, H. ET. AL., "Model Predictive Control of an Autonomous Blimp with Input and Output Constraints", *Proceedings of the 2006 IEEE International Conference on Control Applications, Munich* Germany, 2006.

[4] YAMASAKI, T., FUJITA, H., GOTO, N., "Identification of Blimp Dynamics by Indoor Free Flight Test", AIAA-2002-4405, *AIAA Atmospheric Flight Mechanics Conference and Exhibition*, Monterey, Ca., 2002.

[5] KORNIENKO, A., "System Identification Approach to Determining Flight Dynamical Characteristics of an Airship from Flight Data", Stuttgart University Ph.D. Dissertation, 2006.

[6] LI, Y., "Dynamics Modeling and Simulation of Flexible Airships", McGill University Ph.D. Dissertation, 2008.

[7] LAMB, Sir H., Hydrodynamics, Dover, New York, 6th Edition, 1945.

[8] MUNK, M. M., "The Aerodynamic Forces on Airship Hulls", Report No. 184, National Advisory Committee of Aeronautics, 1924.

[9] SAGATUN, S., FOSSEN, T. I., "Lagrangian Formulation of Underwater Vehicles' Dynamics", IEEE, 1992.

[10] KHOURY, G., GILLETT, J. Airship Technology, 1999.

[11] SALAMA, M., LOU, M., FANG, H., "Deployment of Inflatable Space Structures: A Review of Recent Developments", AIAA-2000-1730, American Institute of Aeronautics and Astronautics, 2000.

[12] JUNKINS, J. , KIM, Y. Introduction to Dynamics and Control of Flexible Structures, AIAA Educational Series, 1993.

[13] KOLODNY, M. A., "Initial Experiment in Using a Powered Parafoil for Employment of Intelligence, Surveillance, and Reconnaissance (ISR) Unattended Ground Sensors (UGS)", Army Research Lab Technical Report, 2004.

[14] CARTER, D. W., "Autonomous Large Parafoil Guidance, Navigation and Control System Design Status", *19th AIAA Aerodynamics Decelerator Systems Technology Conference and Seminar,* Williamsburg, VA, 2007.

[15] SLEGERS, N., COSTELLO, M., "Aspects of Control for a Parafoil and Payload System", AIAA Journal of Guidance, Control and Dynamics, Vol 26, No. 6, 2003.

[16] SLEGERS, N., "Effects of canopy-Payload Relative Motion on Control of Autonomous Parafoils", AIAA Journal of Guidance, Control and Dynamics, Vol, 33, No. 1, 2010.

[17] MAIN, J. A., PETERSON, S. W., STRAUSS, A. M., "Load-Deflection Behavior of Space-Based Inflatable Fabric Beams", American Society of Civil Engineers (ASCE) Journal of Aerospace Engineering, Vol. 7, No. 2, 1994.

[18] RAGHAVAN, B., "Flight Dynamics and Control of Highly Flexible Flying-Wings", Virginia Tech, Ph.D. Dissertation, 2009.

[19] WIELGOSZ, C., THOMAS, J. C., CASARI, P., "Strength of Inflatable Fabric Beams at High Pressure", *Presented at the 43rd AIAA/ASME/ASCE/AHS/ASC Structures, Structural Dynamics, and Materials Conference*, Denver, Colorado, 2002.

[20] SU, W., CESNIK, C., "Dynamic Response of Highly Flexible Flying Wings", AIAA 2006-1636, *Presented at the 47th AIAA/ASME/ASCE/AHS/ASC* 2006.

[21] PATIL, M., HODGES, D., "Flight Dynamics of Highly Flexible Flying Wings", *Proceedings of the International Forum on Aeroelasticity and Structural Dynamics,* Music, Germany, 2005.

[22] "Aerovironment, UAS: Puma AE", http://www.avinc.com/uas/small_uas/puma/, Profile page, (Accessed April 4th, 2010) .

[23] TUZCU, I., MEIROVITCH, L. “Effects of Flexibility on the Stability of Flying Aircraft”, ASME Journal of Dynamics Systems, Measurement and Control, 2005.

[24] ETKIN, B., Dynamics of Atmospheric Flight*, Wiley,* 1972.

[25] BENNACEUR, S., BICHOU, A., AZOUZ, N., “Modeling and Control of Flexible Airships”, *Intelligent Systems and Automation, 1st Mediterranean Conference,* 2008.

[26] “ILC Dover: UAV Wings”, http://www.ilcdover.com/UAV-Wings/, Profile page, (Accessed November 12th, 2009) .

[27] REASOR, D., LEBEAU, R., “Numerical Investigation of the Effects of Bumps on Inflatable Wing Profiles”, *AIAA Region III Student Conference, South Bend, IN,* 2007.

[28] CADOGAN, D., ET AL., “Recent Development and Test of Inflatable Wings”, AIAA-2006-2831, 47th AIAA/ASME/ASCE/AHS/ASC Structures, Structural Dynamics, and Materials Conference, Newport RI, 2006.

[29] JACOB, J. D., SIMPSON, A., SMITH, S., “Design and Flight Testing of Inflatable Wings with Wing Warping”, SAE 05WAC-61, 2005.

[30] ROWE, J. et. al., “Development of a Finite Element Model of Warping Inflatable Wings”, *47th AIAA/ASME/ASCE/AHS/ASC Structures, Structural Dynamics, and Materials Conference,* Newport RI, 2006.

[31] TAM, D. ET. AL., “Tumbling Dynamics of Flexible Wings”, MIT, 2009.

[32] CHANG, C.W.C., *Conceptual Design and Realization of An Inflatable Uninhabited Aerial Vehicle*, Master's Thesis, The Imperial College of London, 2005.

[33] RESKHE, C., *Integrated Flight Loads Modeling and Analysis for Flexible Transport Aircraft*, Ph.D. Dissertation, Stuttgart University, 2006.

[34] PATIL, M., *Nonlinear Aeroelastic Analysis, Flight Dynamics, and Control of a Complete Aircraft,* Ph.D. Thesis, Georgia Institute of Technology, 1999.

[35] SHEARER, C.M., *Coupled Nonlinear Flight Dynamics, Aeroelasticity, and Control of Very Flexible Aircraft*, Ph. D. Disseration, University of Michigan, 2006.

[36] LOOYE, G.H.N, *An Integrated Approach to Aircraft Modeling and Flight Control Law Design*, Ph. D. Disseration, TU Delft, 2007.

[37] REIJERKERK, M. J., *Aeroelastic Model Identification of Winglet Loads from Flight Data*, Ph.D. Dissertation, TU Delft, 2008.

[38] WASZAK, M. R., SCHMIDT, D. K.., "Flight Dynamics of Aeroelastic Vehicles", AIAA Journal of Aircraft, Vol. 25, No 6, June 1988.

[39] CHANG, C-S, "Vibration and Aeroelastic Analysis of Highly Flexible HALE Aircraft", Georgia Tech, Ph.D. Dissertation, 2006.

[40] SU, W, *Coupled Nonlinear Aeroelasticity and Flight Dynamics of Fully Flexible Aircraft,* Ph.D. Dissertation, University of Michigan, 2008.

[41] LI, Y., NAHON, M., "Modeling and Simulation of Airship Dynamics", AIAA Journal of Guidance, Control and Dynamics, Vol. 30, No. 6, 2007.

[42] SIMPSON, A. ET. AL., "Flight Control of a UAV with Inflatable Wings with Wing Warping".

[43] SHEARER, C. M., and CESNIK, C. E. S., "Trajectory Control for Very Flexible Aircraft," Journal of Guidance, Control, and Dynamics, Vol. 31, No. 2, 2008.

[44] AZINHEIRA, J-S., ET. AL., "Influence of Wind Speed on Airship Dynamics", Journal of Guidance, Control and Dynamics, Vol. 25, No. 6, 2002.

[45] PALACIOS, R., CESNIK, C., "Structural Models for Flight Dynamics Analysis of Very Flexible Aircraft", Presented at the 50th AIAA/ASME/ASCE/AHS/ASC Structures, Structural Dynamics, and Materials Conference, Palm Springs, Ca, 2009.

[46] GILBERT, M. G., *Dynamic Modeling and Active Control of Aeroelastic Vehicles*, Master's Thesis, Purdue University, 1982.

[47] SCHMIDT, D. K. , RAINEY, D. L., "Modeling and Simulation of Flexible Flight Vehicles", AIAA Journal of Guidance, Control and Dynamics, Vol 24. No. 3, 2001.

[48] PETERS, D. A., ET. AL., "Finite State Induced Flow Models Part I: Two-Dimensional Thin Airfoil", AIAA Journal of Aircraft, Vol. 37, No. 2., 1995.

[49] HODGES D. H., PIERCE, G. A. Introduction to Structural Dynamics and Aeroelasticity, Cambridge University Press, 2006.

[50] SLEGERS, N., "Effects of canopy-Payload Relative Motion on Control of Autonomous Parafoils", AIAA Journal of Guidance, Control and Dynamics, Vol, 33, No. 1, 2010.

[51] BARROWS, T. M., "Apparent Mass of Parafoils with Spanwise Camber", AIAA Journal of Aircraft, Vol. 39, No. 3, 2002.

[52] LISSAMAN, P.B.S., "Apparent Mass Effects on Parafoil Dynamics", AIAA paper 93-1241, 1993.

[53] WASZAK, M. R., SCHMIDT, D. K., "A Simulation Study of the Flight Dynamics of Elastic Aircraft", *Vol I & II*, NASA Contractor Report, 1987.

[54] CROSBIE, ET. AL. "Computational Aerodynamics and Experimental Investigations of an Inflatable Wing", *Presented at the 8th International Conference on Computational Structures Engineering,* Las Palmas de Gran Canaria, Spain, September 2006.

[55] COFFIN, P. B., SINGER, C.L., "Overview of Inflatable UAV Research at Clarkson University", Clarkson University, 2008.

[56] "Cubic Tech, Products", http://www.cubictechnology.com/Products.html, *(*Accessed April 5th, 2010).